The Impact of Sintered Ag-Al Interconnects on the Power Cycling Reliability of Die Attachments

Fupeng Huo, Chuantong Chen, *Senior Member, IEEE,* Zheng Zhang, *Member, IEEE*, Sangmin Lee, Dongjin Kim, *Member, IEEE,* Yicheng Zhang, Aiji Suetake, Takeshita Kazutaka, Yoshiji Yamaguchi, Yashima Momose, Katsuaki Suganuma, *Senior Member, IEEE*

***Abstract*—In this study, the degradation behavior of mimicked power modules with silicon carbide (SiC)/sintered silver (Ag)/direct bonded aluminum (DBA) structure was investigated during power cycling under a junction temperature of 200°C. To mitigate this degradation, a sintered Ag composite paste doped with micron-sized Al particles (sintered AgAl) was specifically developed for DBA substrates, leading to the proposed SiC/sintered AgAl/DBA structure. Power cycling results demonstrated that the degradation was effectively suppressed, attributed to the reduced coefficient of thermal expansion (CTE) mismatch between sintered layer and DBA substrate, as well as robust bonding among sintered Ag, DBA substrate, and Al particles. The SiC/sintered Ag/DBA mimicked power module failed after 9200 cycles. Compared to the initial values, transient thermal resistance and junction temperature increased by 39.9% and 123.0%, respectively. In contrast, for the SiC/sintered Ag15Al/DBA structure, the crack density is reduced and the crack spacing increased from 71.6 to 154.1 μm. CTE mismatch was also reduced from 12.4 × 10^{-6}/K to 1.8 × 10^{-6}/K at 200°C. the newly developed SiC/sintered Ag15Al/DBA structure exhibited only a 0.5% and 7.6% increase in transient thermal resistance and junction temperature, respectively, after 10000 cycles. The results are significantly lower than that of SiC/sintered Ag/DBA structure.**

***Index Terms*—Power module, sintered AgAl composite paste, DBA substrate, real-time thermal monitor, power cycling reliability.**

I. INTRODUCTION

Wide bandgap semiconductor, silicon carbide (SiC), has attracted significant attention due to its exceptional properties, such as high critical breakdown electric field and high thermal conductivity [1-3]. It demonstrates great potential in applications such as electric vehicles, high-speed rail, 6G communications, and aerospace [4,5]. With the miniaturization and increasing power of SiC power modules, junction temperatures have risen to 200°C [6]. The substantial heat generated by SiC power modules is dissipated to the heat sink via the die attach layer and substrate layer (directed bonded copper (DBC), directed bonded aluminum (DBA)). In this case, the die attach/substrate structure serves as critical pathways for heat dissipation in high-power modules. Therefore, it is essential to develop die attach/substrate structure that are both high-temperature resistant and highly reliable.

Traditional tin-based (Sn-based) solders are unsuitable for the demands of SiC power modules due to their low melting points [7]. To solve this issue, many candidates have been proposed, including the transient liquid phase (TLP) method [8], sintered nano silver (Ag), copper (Cu) [9,10], as well as high-temperature solder alloys [11]. Recently, nano Cu sintering has attracted widespread attention due to its significantly lower material cost (less than 10% of nano silver paste), lower ion migration tendency, high melting point (enabling operation above 250 °C), and excellent thermal conductivity (398 W/(m·K) for bulk Cu) [12,13]. However, sintered Cu is prone to oxidation and thus requires complex processing conditions [14]. Among these, sintered nano Ag is regarded as the most promising die attach material due to its excellent thermal conductivity, electrical conductivity, and mechanical properties [15,16]. However, sintered nano Ag presents challenges, including high manufacturing and storage costs resulting from its high specific surface area. Specific surface area refers to the total surface area of a material per unit mass or unit volume [17]. It is inversely proportional to the particle radius. That is, the smaller the particle radius, the larger the specific surface area. Additionally, the pressure assisted sintering process places specific demands on die attach equipment [18]. Furthermore, nano sintered Ag suffers from microstructural coarsening, which may affect the reliability of power modules [19]. To address these issues, our laboratory developed a micron Ag paste that enables low-temperature (250°C), pressureless sintering in air atmosphere and demonstrates good high-temperature reliability [20-22].

In addition to the die attach layer, the substrate component is also a critical factor influencing the reliability of power modules. The reliability issues of the commonly used DBC substrate have been extensively studied [23-25]. On the one hand, the reliability issues arise from the oxidation of Cu; the bonding between sintered Ag and DBC substrate essentially forms a copper oxide (CuO)-Ag interface, where the CuO

This work was supported by a project (JPNP20004) commissioned by the New Energy and Industrial Technology Development Organization (NEDO) and JSPS KAKENHI Grant Number JP22K04243, and by a research grant from The Murata Science Foundation. *(Corresponding author: Chuantong Chen.)*

Fupeng Huo, Chuantong Chen, Zheng Zhang, Sangmin Lee, Yicheng Zhang, Aiji Suetake, and Katsuaki Suganuma are with the Flexible 3D System Integration Laboratory, The Institute of Science and Industrial Research, Osaka University, Osaka, 567-0047, Japan. (e-mail: huofp@sanken.osaka-u.ac.jp; chenchuantong@sanken.osaka-u.ac.jp; zhangzheng@sanken.osaka-u.ac.jp; s.lee@sanken.osaka-u.ac.jp; yicheng.zhang@sanken.osaka-u.ac.jp; asuetake@sanken.osaka-u.ac.jp; suganuma@sanken.osaka-u.ac.jp).

Dongjin Kim is with the Micro-Joining Center, Korea Institute of Industrial Technology (KITECH), 156 Gaetbeol-ro, Yeonsu-gu, Incheon 21999, Republic of Korea. (dongjinkim@kitech.re.kr)

Takeshita Kazutaka, Yoshiji Yamaguchi, and Yashima Momose are with the Yamato Scientific Co. Ltd., Tokyo, 135-0047, Japan (e-mail: kazutaka.takeshita@yamato-net.co.jp; yamaguchiyo@yamato-net.co.jp; yashima.momose@yamato-net.co.jp).

layer's thickness increases under long-term service operation. This results in an increase in thermal and electrical resistance in the sintered Ag/DBC structure, ultimately leading to power module failure. On the other hand, the high yield strength and strain hardening of Cu, coupled with the CTE mismatch between DBC substrate and sintered Ag, also contribute to the degradation of the interfacial microstructure. To mitigate the oxidation and CTE mismatch of DBC substrate, some researchers have proposed coating the DBC substrate with multilayer metals using chemical plating or sputtering methods [26,27]. Liu et al. [26] prepared nickel/platinum /silver (Ni/Pt/Ag) multilayer metallization on DBC substrate by combining electroplating and electroless plating. The results showed that the microstructural degradation of the sintered joint was suppressed, thereby improving reliability. Xu et al. [27] prepared electroless nickel immersion gold (ENIG) and electroplated nickel/gold (Ni/Au) metallized DBC substrates and studied the interfacial reactions with sintered nano Ag. However, this approach increases costs. In contrast, the aluminum nitride (AlN) ceramic in DBA substrates possesses a higher thermal conductivity than the silicon nitride (Si_3N_4) ceramic used in DBC substrates. In our previous studies [28], the thermal conductivity of the DBA substrate was slightly lower than that of the DBC substrate at low temperatures (approximately 60 °C). However, at elevated temperatures (approximately 200 °C), the thermal conductivities of DBA and DBC substrates became nearly identical, indicating that DBA substrates exhibit excellent thermal conductivity stability. Moreover, DBA substrates offer the advantage of lightweight, which is particularly beneficial for high-power and weight-sensitive applications. Additionally, the aluminum layer in DBA substrates exhibits superior plastic deformability compared to Cu, enabling stress relaxation and enhancing thermal shock reliability, which also was validated by our prior research [29]. Due to the good deformability of Al, stress is absorbed by plastic deformation. For the DBC substrate, it behaves longer elastically, the degradation itself is less. However, for the sintered Ag/DBC structure, delamination occurs at the interface, making the overall degradation more obvious. The shear strength of sintered Ag/DBC structure almost decreased to zero after 250 thermal shock cycles. On the other hand, compared to active metal brazed (AMB) substrate, DBA substrate also exhibits superior thermal cycling reliability. Hamilton et al. [30] conducted thermal cycling reliability evaluations on AMB (Si_3N_4 core) and DBA (AlN core) substrates. It found that the AMB (Si_3N_4 core) substrate failed after 640 cycles within a 0–350 °C temperature range, whereas the DBA (AlN core) substrate remained failure-free after 990 cycles. Therefore, DBA substrates are especially suitable for high-power electronics. In recent years, with the rapid development of wide bandgap semiconductors, power modules featuring sintered Ag/DBA structures have demonstrated immense market potential for high-power electronics.

However, the naturally occurring alumina (Al_2O_3) film on the surface of DBA substrates poses challenges for bonding with sintered Ag [31]. Recently, our research team achieved robust bonding between micron sintered Ag and DBA substrate, reaching a shear strength of 33.6 MPa under pressureless sintering conditions [32], significantly exceeding the MIL-STD-883 K standard (7.8 MPa) [33]. However, the underlying bonding mechanism remains unclear. In addition, in reliability tests, the sintered Ag/DBA structure has exhibited good thermal aging performance. However, significant microstructural degradation was observed during power cycling tests, which more closely simulate real operating conditions [32]. Power cycling primarily assesses the aging effects caused by the CTE mismatch of different packaging materials under cyclic thermal stress [34]. Therefore, CTE mismatch is considered the primary cause of the degradation observed in sintered Ag/DBA structures. To address this issue, die attach materials specifically designed for DBA substrates need to be developed.

To enhance the performance of sintered Ag, two approaches are generally employed: one involves the incorporation of ceramic particles to form composite pastes, and the other is metal alloying. The addition of ceramic particles significantly reduces thermal and electrical conductivity of Ag [35]. Moreover, most ceramic particles have relatively low CTE (typically 10^{-6}/K [36]). Their inclusion further decreases the CTE of the sintered Ag layer, increasing the CTE mismatch with the DBA substrate, thereby accelerating microstructural degradation. In contrast, metal doping is considered a more suitable approach. Candidate metals include Cu, indium, and Al [8,37,38]. The addition of Cu can result in the formation of a supersaturated Ag-Cu solid solution paste; however, oxidation issues persist. While doping with indium can improve microstructural stability and shear strength, its high cost is a major drawback. Furthermore, intermetallic compounds (IMC) tend to form during long-term service, which compromises the reliability of the joint. On the other hand, Al particles offer distinct advantages. Due to the presence of a native Al_2O_3 layer on the surface, it exhibits a core–shell structure that suppresses the formation of IMC between Al and Ag during long-term service. In previous studies [32], the degradation of the sintered Ag/DBA structure was primarily attributed to the CTE mismatch. Specifically, the lower CTE of sintered Ag compared to the DBA substrate. Incorporating Al particles into sintered Ag increases the CTE of sintered AgAl layer, thereby reducing the CTE mismatch with the DBA substrate.

In this study, we systematically investigated the degradation behavior of the SiC/sintered Ag/DBA structure. In particular, the interface bonding mechanism between Ag and DBA substrate during power cycling was systematically explained. Additionally, to mitigate microstructural degradation, the micron Al particle doped sintered Ag composite paste (sintered AgAl) was specifically designed for DBA substrate. A SiC/sintered AgAl/DBA structured mimicked power module was proposed. These findings are expected to provide experimental foundations for developing highly reliable SiC/sintered AgAl/DBA structured power modules.

II. Experiment

A. Preparation of sintered AgAl composite paste

The micron sized Ag flakes were jointly developed by our laboratory and Fukuda Metal Foil and Powder Ltd., Kyoto,

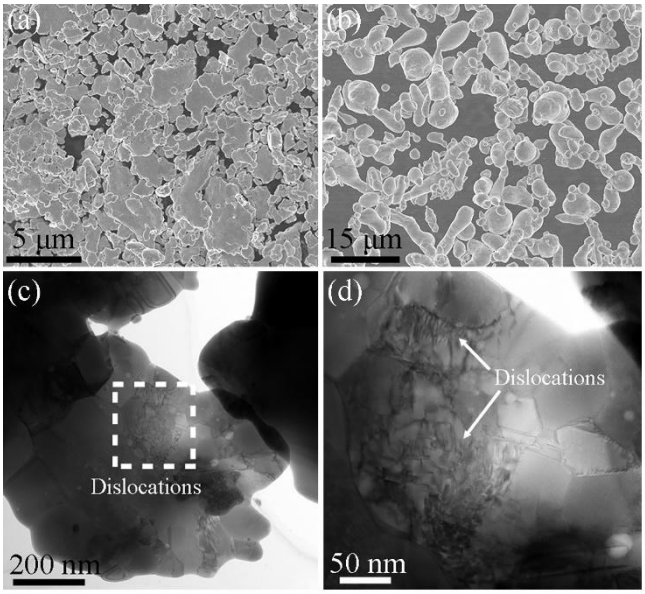

Fig. 1 Morphology of Ag flake and Al particles. (a) SEM image of Ag flake. (b) SEM image of Al particles. (c) TEM image of Ag flake. (d) High-magnification of Fig. 1(c).

Japan. The scanning electron microscopy (SEM, SU8020, Hitachi, Japan) image is depicted in Fig. 1(a), revealing planar dimensions ranging from 0.5 to 6.1 μm, with an average size of 1.6 μm. The thickness ranges from 0.3 to 0.5 μm, with an average of 0.4 μm. Fig. 1(c) shows a transmission electron microscopy (TEM, JEM-ARM200F, JEOL, Japan) image of the Ag flakes. The micron sized Ag flakes consist of nanoscale grains, with an average grain size of 71.3 nm. Additionally, high-density dislocations are observed, as marked by the dotted box. The high-magnification image of Fig. 1(c) is shown in Fig. 1(d). These dislocations intertwine to form tangles and splices. This phenomenon is attributed to the unique ball milling preparation method used for the Ag flakes. The micron sized Al particles were supplied by the Institute for Materials Research, Saitama, Japan. As shown in Fig. 1(b), the particles exhibit spherical, ellipsoidal, and short rod shapes, with sizes ranging from 0.6 to 8.5 μm and an average size of 3.2 μm. The organic solvent CELTOL-IA was supplied by Daicel Corporation, Kyoto, Japan.

First, Ag flakes and Al particles were mixed in specific ratios, with the mass fractions of Al particles being 0, 5 wt.%, 10 wt.%, and 15 wt.%, respectively. The mixed powders were thoroughly blended with 10 wt.% CELTOL-IA using a mixing device (ARV-310, THINKY, Japan) to fabricate sintered AgAl composite pastes. Detailed preparation procedure of the AgAl composite pastes has been reported in [38].

B. Real-time Thermal Characteristic Monitoring Instrument

The real-time thermal characteristic monitoring system is a proprietary instrument jointly developed by Yamato Scientific Ltd. and our laboratory [39,40]. This equipment has been certified by the international standard ISO 4825-1: 2023 and serves as a standardized instrument for measuring the thermal properties of power semiconductor modules and packaging materials. As shown in Fig. 2(a), The instrument comprises three main components: control system, power supply, and sample mounting platform. Among them, the control system is a python-based program capable of performing following functions: setting the switch-on and switch-off durations during the power cycling, as well as automatically calculating the transient thermal resistance by collecting and analyzing the monitored junction and case temperatures. As for the power supply, it is a DC power source with the model TEXIO PSW-360M160. A magnified view of the sample mounting platform is shown in Fig. 2(b), and its cross-sectional schematic is provided in Fig. 2(c).

On top is the SiC heater chip, a high-density heat source integrated with a temperature sensor. It simulates the heat generated by an active chip and collects temperature data in real time. Below is the die attach layer, which connects the heater chip to the DBA substrate. The DBA substrate is connected to the heat sink via a thermal interface material (TIM, thermal sheet, SHINETSU, Japan). A thermocouple is embedded in the TIM region to monitor the case temperature in real time. The transient thermal resistance value is calculated using Equation (1) [3]:

$$Z_{th} = \frac{T_j - T_c}{P} \quad (1)$$

$$P = U \cdot I \quad (2)$$

where Z_{th} is the transient thermal resistance (K/W), which is from the top of the heater chip to the back of the DBA substrate. T_j is the junction temperature measured by the temperature sensor integrated in heater chip (°C). T_c is the case temperature measured by the thermocouple in the TIM region (°C). P is the input power (W). I is the input current (A), and U is the input voltage (V). Since the control system collects T_j and T_c in real-time, the Z_{th} is simultaneously calculated by embedding Equation (1) in the system.

Moreover, the sample mounting platform is versatile and supports various experimental configurations. For instance, in the die attach layer, materials such as solder, sintered Ag, and sintered Cu can be used to investigate the impact of different die attach materials on the thermal performance and reliability of power modules. In the substrate component, DBC, DBA, and AMB substrates can be used to study the effects of different substrates on transient thermal resistance and reliability. For the heat sink, as shown in Fig. 2(c), a water-cooled heat sink is depicted, but an air-cooled heat sink can also be used. In summary, this is a flexible platform for evaluating the thermal characteristics of mimicked power modules, suitable for diverse applications.

In this instrument, the SiC heater chip plays a critical role as both a high-density heat source and a real-time junction temperature sensor. An n-doped 4H SiC semiconductor with dimensions of 5 × 5 × 0.35 mm³ was utilized as a heater chip, and it can be mass-produced via lithography on an n-doped 4H-SiC wafer [40]. A representative SiC heater chip is shown in Fig. 2(d). The metal pattern on the surface of the heater chip consists of four parts: the heating wire (marked as 1), the heating electrode (marked as 2), the temperature sensor (marked as 3), and the temperature sensor electrode (marked as 4). Part 1 generates heat through a Pt resistive wire to achieve the target junction temperature. Part 2 functions as the power input terminal. Part 3 monitors the temperature of the heater chip, and part 4 inputs a small current (0.1 A). Here, Pt

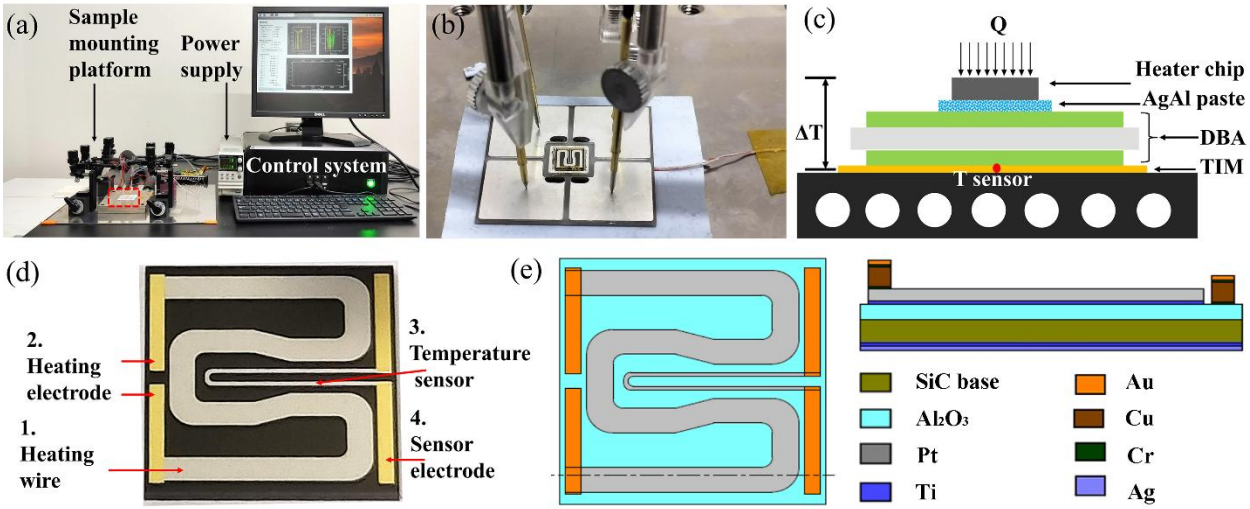

Fig. 2 Real-time thermal characteristic monitoring instrument. (a) Overall view. (b) Magnified view of the sample mounting platform. (c) Cross-sectional schematic of platform. (d) SiC heater chip image. (e) The specific material choices of heater chip.

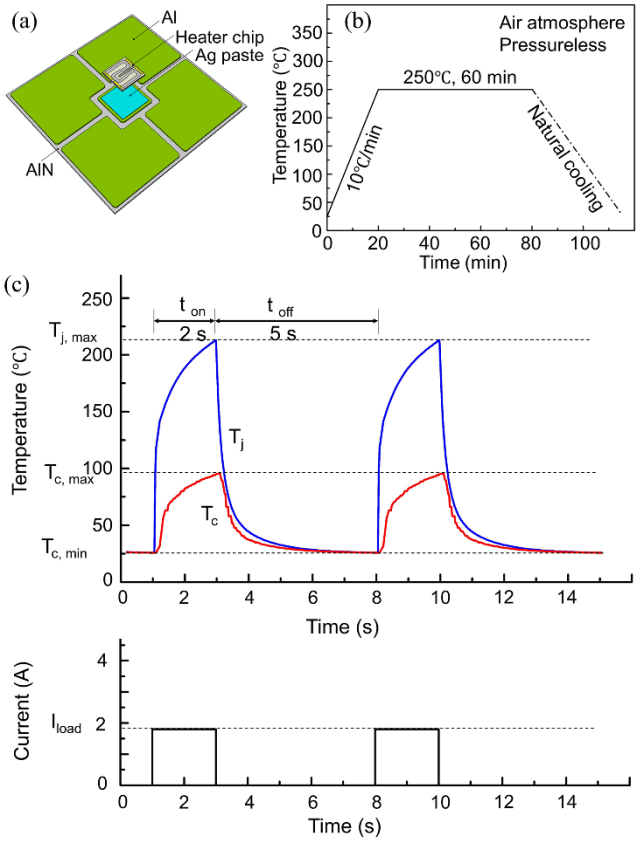

Fig. 3 Bonding and power cycling program. (a) The schematic diagram of bonding program. (b) Sintering profile. (c) Representative temperature and input current profiles.

is used to fabricate the pattern due to its excellent thermal stability and resistance to electromigration [41,42]. Under the pattern is a 1 μm thick Al_2O_3 insulation layer, which is employed to uniformly generate heat and prevent electrical short circuits. titanium (Ti) and Ag films are sputtered onto the backside of the SiC chip to facilitate bonding with the die attach layer. Material specifications and dimensions are provided in Fig. 2(e). For pattern fabrication, the Pt thin film, including the heater and sensor, was sputtered onto the Al_2O_3 layer using lithography. The electrodes were formed by multi-sputtering of Ti/Cu/Ti/Au layers through a pre-designed metal mask.

C. Thermal Characteristic Monitoring During Power Cycling

First, pure Ag and AgAl composite pastes were printed on DBA substrate with a thickness of 100 μm. The SiC heater chip was subsequently mounted onto the printed paste layer. A schematic diagram of the structure is shown in Fig. 3(a). The TG-DTA curves of the Ag and AgAl pastes are shown in Fig. S1. The addition of Al particles has little effect on the TG-DTA curve of the Ag paste, indicating that the sintering processes for both Ag and AgAl pastes are compatible. Based on this observation, the corresponding sintering process was developed. The sintering profile is illustrated in Fig. 3(b). Sintering temperature was 250°C, maintained for 60 min, no pressure applied during the entire process. The sintered SiC heater chip/DBA structure was mounted onto a water-cooled heat sink using TIM. The heat sink temperature was maintained at 25°C. The DBA substrate was supplied by Mitsubishi Materials Co., Japan.

According to the power electronics guideline AQG-324 [43], second-level power cycling is required to evaluate the power cycling reliability of die attachment materials. The standard specifies that the switch-on time should be less than 5 seconds. In this study, the switch-on time was set to 2 seconds because a junction temperature of 200 °C could be reached within this duration. The switch-off time was set to 5 seconds to allow the heater chip temperature to return to room

TABLE I POWER CYCLING TEST CONDITIONS

Paste	P (W)	U (V)	I (A)	Max Tj (°C)	Switch on (s)	Switch off (s)	Swing temperature (°C)
Ag	122.97	66.83	1.84	200	2	5	175
Ag5Al	116.57	64.05	1.82	200	2	5	175
Ag10Al	109.33	61.42	1.78	200	2	5	175
Ag15Al	105.78	60.79	1.74	200	2	5	175

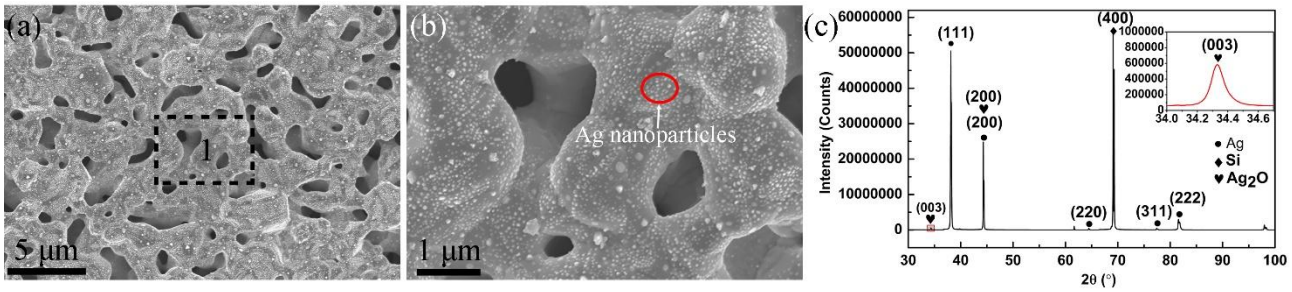

Fig. 4 SEM and XRD results of sintered Ag. (a) Surface morphology of sintered Ag with pressureless condition. (b) High-magnification image of area 1 in Fig. 4(a). (c) XRD of sintered Ag.

temperature (25 °C). Power cycling conditions are listed in Table 1. During testing, with the input specified power, chip's junction temperature reached 200°C, with a temperature swing (ΔT_j) of 175°C. Representative profiles of temperature and input current are shown in Fig. 3(c). First, power cycling was conducted on the SiC heater chip/sintered Ag/DBA structure for 0, 3000, and 10,000 cycles to evaluate the degradation of joint microstructure and real-time thermal characteristics. Subsequently, SiC heater chip/DBA structures sintered with different AgAl paste compositions were tested at a junction temperature of 200°C for 10000 power cycles. During the test, if the heater chip fails, the power cycling test will automatically stop. Finally, to evaluate the lifetime of AgAl composite paste sintered power modules, long-term power cycling tests were also conducted. According to the power electronics guideline (AQG-324) [43], the power cycling lifetime was defined as the cycle number where Z_{th} reached 120% of the initial Z_{th} during the power cycling test.

D. Characterization and Testing

The surface morphology of the pressureless sintered Ag paste was examined using SEM. X-ray diffraction (XRD, SmartLab, RIGAKU, Japan) was used to analyze the phase composition after sintering.

X-ray computed tomography (CT) was used to examine crack in the SiC/sintered Ag/DBA structure before and after power cycling. The microstructure was observed through SEM, with samples prepared using ion-milling system (IM4000, Hitachi, Japan). The interfaces between the sintered Ag and DBA substrate, and Al particles within the sintered AgAl paste layer, were systematically studied using TEM.

Microstructural degradation during power cycling is attributed to the CTE mismatch. The CTE of sintered AgAl materials was measured using the mechanical dilatometry method. The principle involves mechanically transmitting thermal expansion-induced displacement to a remote sensor, generating a displacement–temperature plot from which the CTE is calculated [44]. The CTE measurements were conducted using a thermomechanical analysis apparatus (TMA-60, Shimadzu Corporation, Japan). First, The AgAl paste was compacted into an 8 mm diameter mold and sintered following the process in Fig. 3(b). Then, the sintered samples were polished to a final thickness of 1.5 mm and diameter of 8 mm. Testing was performed from 25°C to 350°C under nitrogen atmosphere with a heating rate of 5°C/min. In addition to the sintered AgAl paste, the CTE of the DBA substrate was also tested under the same condition. Additionally, the resistivity of the sintered AgAl composite pastes were measured using a four-point probe method (MCP T610, Loresta-GP, Mitsubishi Chemical). The resistivity sample was prepared using the same sintering process described in Fig. 3(b). The final dimensions of the specimen were 35 mm × 10 mm × 0.1 mm (length × width × height). The resistivity result is the average of 4 measurements.

III. Results

A. Microstructure Evolution of SiC/ Sintered Ag/DBA Structure During Power Cycling

Fig. 4(a) shows the surface morphology of sintered Ag with pressureless condition, which reveals a typical porous structure indicative of good sintering performance. The high-magnification image of area 1 in Fig. 4(a) is shown in Fig. 4(b), revealing numerous nanoparticles (marked with red circle). This phenomenon is rarely reported and suggests that nanoparticles precipitated from the micron sized Ag flakes during sintering [45,46]. XRD analysis was conducted to identify the phase of these nanoparticles. As shown in Fig. 4(c), the XRD results reveal the presence of Ag, Si (the substrate used for XRD), and Ag_2O. This indicates that the nanoparticles are composed of Ag_2O. Previous studies [38] using in-situ TEM revealed the ejection of ultra-fine Ag nanoparticles from Ag flakes under electron beam irradiation. Ag flakes, prepared through high-energy ball milling, retain significant amount of stored energy within their structure. At this stage, the Ag flakes are in a metastable state. When subjected to external energy (such as heating or irradiation) to overcome the energy barrier, the stored energy is released in the form of nanoscale Ag amorphous particles being ejected. With a continuous supply of heat, the amorphous Ag particles gradually transform into nanocrystals. This unique ejection phenomenon of Ag nanoparticles from Ag flakes facilitates the low-temperature pressureless sintering of micron sized Ag, which acts as a bridge for micron Ag flake sintering interconnection. This also explains the presence of nanoparticles observed in Fig. 4(b). The Ag_2O detected in Fig. 4(c) results from the oxidation of ultra-fine Ag nanoparticles during air sintering. More importantly, this phenomenon enables in-situ surface modification of both Al particles and the DBA substrate.

During power cycling, the CTE mismatch between SiC, die attach layer, and DBA substrate leads to the formation of numerous cracks, ultimately reducing the reliability of the

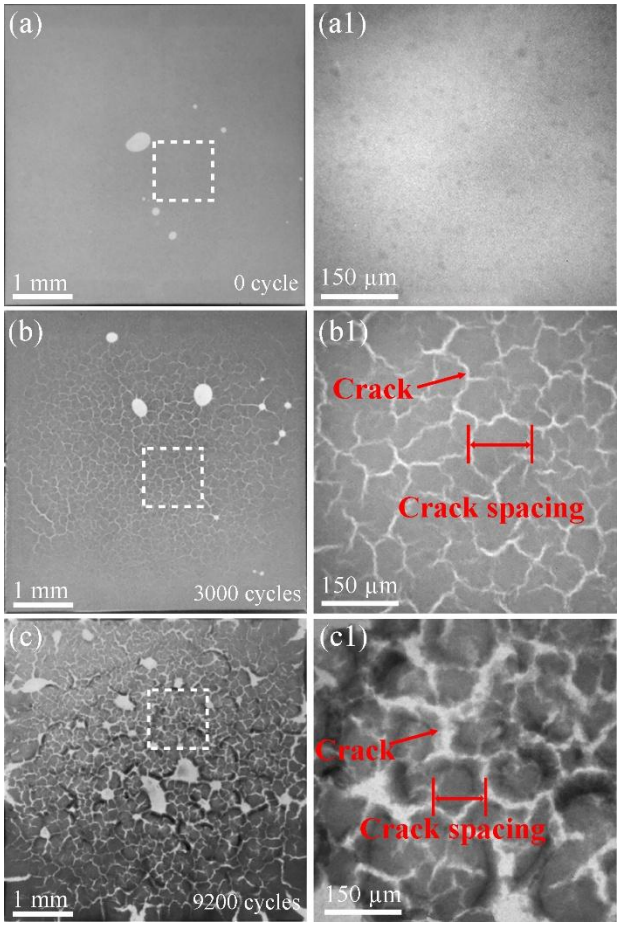

Fig. 5 The CT results of sintered Ag/DBA joints with various power cycles. (a) 0 cycle, (a1) high-magnification of Fig. 5(a). (b) 3000 cycles, (b1) high-magnification of Fig. 5(b). (c) 9200 cycles, (c1) high-magnification of Fig. 5(c).

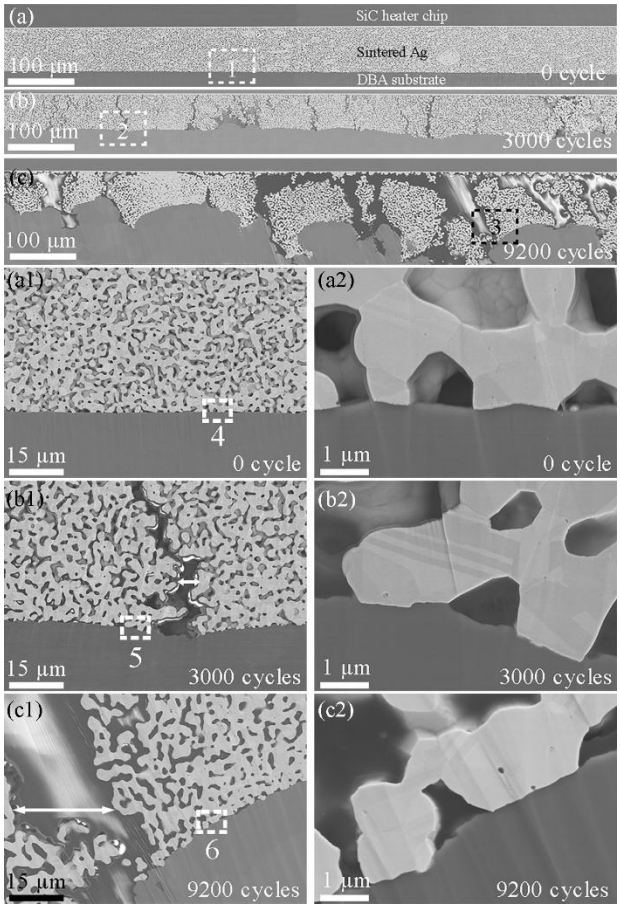

Fig. 6 SEM images of sintered Ag/DBA joints with various power cycles. (a) 0 cycle. (b) 3000 cycles. (c) 9200 cycles. High-magnification image of (a1) area 1 in Fig. 6(a), (b1) area 2 in Fig. 6(b), and (c1) area 3 in Fig. 6(c). High-magnification image of (a2) area 4 in Fig. 6(a1), (b2) area 5 in Fig. 6(b1), and (c1) area 6 in Fig. 6(c1).

joint [47]. To make full view of crack in sintered Ag/DBA joint during different power cycling, CT was conducted. Fig. 5 shows the CT results of the sintered Ag/DBA joint after different power cycling durations. Fig. 5(a) presents the overall view at the initial stage, revealing a few pores. The corresponding high-magnification view in Fig. 5(a1) also confirms the absence of cracks. After 3000 cycles of power cycling (Fig. 5(b)), numerous cracks were observed. The high-magnification view of the dashed box in Fig. 5(b) is shown in Fig. 5(b1), where the white lines represent longitudinal cracks. Statistical analysis showed that the average spacing between cracks was 91.6 μm. Fig. 5(c) displays the CT image after 9200 power cycles. During power cycling, due to the progressive degradation of the microstructure, the heat generated by the heater chip could not be effectively dissipated, ultimately leading to the failure of the Pt pattern of SiC heater chip. As shown in Fig. 5(c), the crack density further increased after 9200 cycles. At this stage, the average crack spacing was 71.6 μm. Additionally, in comparison to Figs. 5(b) and (b1), the white lines in Figs. 5(c) and (c1) appear sharper and wider, suggesting increased crack width and more severe degradation of the SiC/sintered Ag/DBA power module.

To further investigate the microstructure evolution in the sintered Ag/DBA joint during power cycling, SEM were conducted. Fig. 6(a) shows the sintered Ag/DBA joint at the initial stage, consisting of three parts: the SiC heater chip, sintered Ag layer, and DBA substrate. The sintered Ag layer exhibits a uniform porous structure, showing effective sintering. The DBA substrate also exhibited a flat profile, indicating that almost no plastic deformation occurred during the bonding process. This can be attributed to the appropriate low-temperature, pressureless sintering process. The sintered Ag layer is well-bonded to the SiC heater chip, which is attributed to the Ag sputtered on the backside of the SiC heater chip, resulting in an Ag-to-Ag interface. However, bonding between the sintered Ag layer and the DBA substrate requires special attention due to the well-known difficulty of bonding Al. In the low-magnification image (Fig. 6(a)), the sintered Ag layer is well-bonded to the DBA substrate, with no visible pores or gaps, indicating good wetting behavior. The enlarged view of area 1 in Fig. 6(a) is shown in Fig. 6(a1), and the enlarged view of area 4 in Fig. 6(a1) is shown in Fig. 6(a2). Combining them, these images demonstrate that the sintered Ag necks are effectively bonded to the DBA substrate at the microscale.

After 3000 cycles (Fig. 6(b)), numerous longitudinal cracks were observed in the sintered Ag layer, some of which were through-cracks while others were partial. Additionally, the Al layer in the DBA substrate changed from flat to undulated,

indicating significant plastic deformation of both the substrate and the sintered Ag layer. At this stage, no obvious cracks have been observed; however, the deformed region of the DBA substrate corresponds to the area where longitudinal cracks occur in the sintered layer. Interestingly, no transverse cracks were observed in the interface between the sintered Ag layer and the DBA substrate, despite severe deformation in the interface region. In general, crack formation during power cycling is primarily caused by CTE mismatch, leading to both longitudinal and transverse cracks. Longitudinal cracks are primarily caused by the significant CTE mismatch among the SiC chip, sintered Ag layer, and DBA substrate. This mismatch generates substantial shear stress during power cycling, promoting the initiation of longitudinally oriented cracks [48–50]. Consequently, longitudinal cracks tend to form in the early stages of power cycling. In contrast, transverse cracks typically develop after the initiation of longitudinal cracks. These result from accumulated fatigue damage under cyclic stress, which drives crack propagation in the transverse direction [51–53]. At the current stage of 3000 cycles, the accumulated fatigue damage has not reached the critical threshold for transverse crack formation; thus, only longitudinal cracks are present. The average spacing between longitudinal cracks was measured to be 93.2 μm, consistent with the CT results shown in Fig. 5. The enlarged view of area 2 in Fig. 6(b) is shown in Fig. 6(b1). Compared to the initial stage, the sintered Ag microstructure became coarser due to thermal effects and high-frequency plastic deformation during power cycling, which promoted Ag atom diffusion and led to porous structure coarsening. Additionally, the average crack width after 3000 cycles was 4.6 μm. The enlarged view of area 5 in Fig. 6(b1) is shown in Fig. 6(b2). Despite significant plastic deformation in the sintered Ag and DBA substrate, the sintered Ag necks remained well-bonded to the DBA substrate, indicating a robust bonding.

After 9200 cycles (Fig. 6(c)), the sintered Ag layer exhibited severe degradation. Continuous Ag regions were segmented into isolated blocks by longitudinal cracks, and some areas showed collapse and delamination, significantly compromising the reliability of power devices. At this stage, in the transverse cracks were also observed, which can be attributed to fatigue damage caused by cyclic stress [51]. The formation mechanism of transverse cracks can be divided into three stages. The first stage is the stress accumulation. During the switch-on period, current is applied to the SiC heater chip, generating heat and causing both the SiC and the DBA substrate to thermally expand. However, due to the higher thermal expansion of the DBA substrate compared to the SiC chip, the sintered Ag layer is subjected to tensile stress in the transverse direction. Conversely, during the switch-off period, as the temperature drops, the sintered layer experiences transverse compressive stress. The second stage is plastic deformation and damage accumulation. Although the sintered Ag layer has a certain degree of ductility, its microstructure contains nano-voids and grain boundaries, which is determined by the sintering process, and it actually behaves as a quasi-brittle material [54]. With increasing power cycling, the repeated tensile-compressive loading induces localized plastic deformation within the sintered Ag layer, initiating

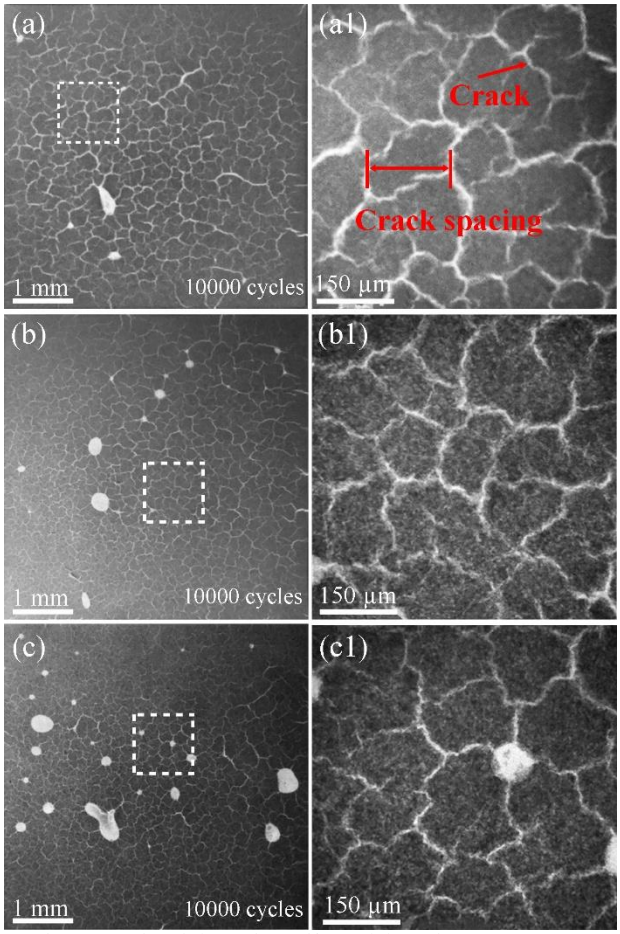

Fig. 7 The CT results of sintered AgAl/DBA joints after 10000 power cycles. (a) Ag5Al, (a1) high-magnification of Fig. 7(a). (b) Ag10Al, (b1) high-magnification of Fig. 7(b). (c) Ag15Al, (c1) high-magnification of Fig. 7(c).

microcracks around voids and grain boundaries [55,56]. The third stage is the crack propagation. As the number of alternating load cycles increases, these microcracks progressively propagate in the direction parallel to the SiC die/DBA interface and eventually form macroscopic transverse cracks. Similarly, the DBA substrate experienced significant deformation, accompanied by the formation of large cracks. The deformation of the DBA substrate is closely correlated with the formation of longitudinal cracks in the sintered layer. The crack spacing in the DBA substrate is almost identical to that in the sintered layer. At this stage, the crack spacing in the DBA substrate is measured to be approximately 73.5 μm. The enlarged view of area 3 in Fig. 6(c) is shown in Fig. 6(c1). Compared to the initial stage, the microstructure of the sintered Ag became increasingly coarse. The average spacing between longitudinal cracks was measured at 73.5 μm, consistent with the CT results in Fig. 5. The average crack width was 27.8 μm, approximately six times greater than after 3000 cycles. The enlarged view of area 5 in Fig. 6(c1) is shown in Fig. 6(c2). Despite severe deformation of the Al layer in the DBA substrate, the sintered Ag layer remained well bonded to it.

In summary, the sintered Ag layer underwent significant degradation during power cycling, evolving from a uniform porous structure to longitudinal cracks and eventually severe fragmentation and collapse. Therefore, although sintered Ag

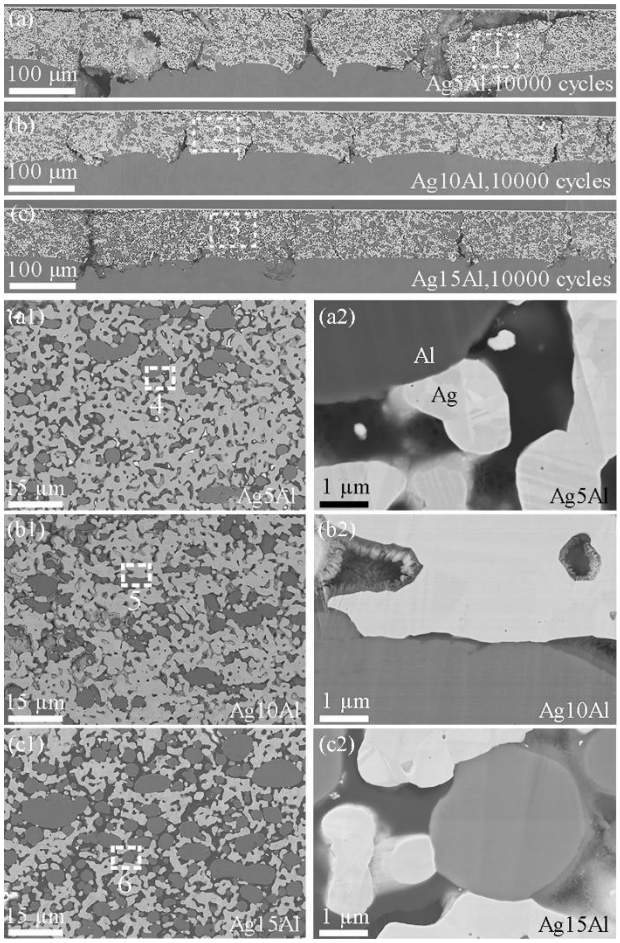

Fig. 8 SEM images of sintered AgAl/DBA joints with varying Al content after 10000 power cycles. (a) Ag5Al. (b) Ag10Al. (c) Ag15Al. High-magnification image of (a1) area 1 in Fig. 8(a), (b1) area 2 in Fig. 8(b), and (c1) area 3 in Fig. 8(c). High-magnification image of (a2) area 4 in Fig. 8(a1), (b2) area 5 in Fig. 8(b1), and (c1) area 6 in Fig. 8(c1).

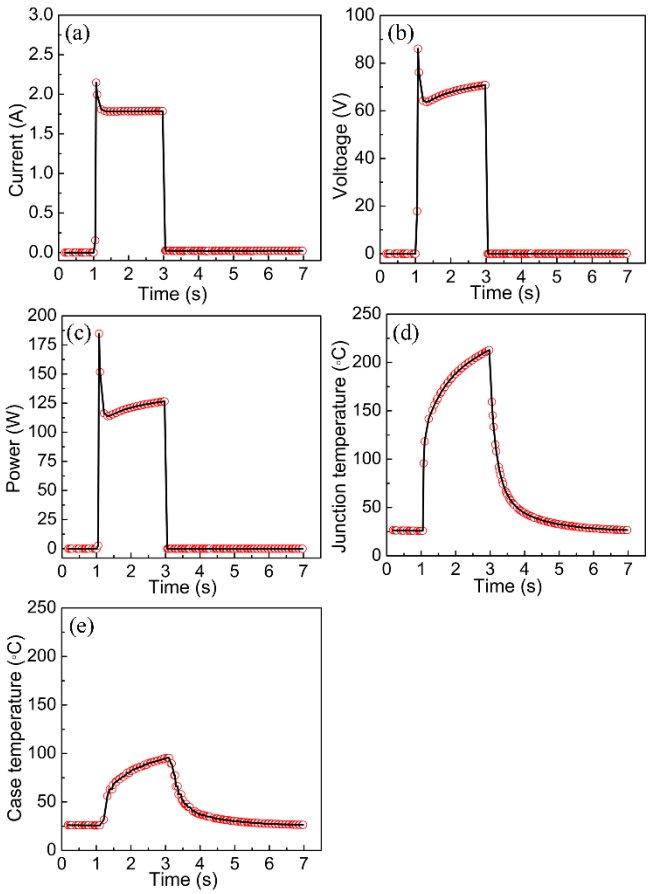

Fig. 9 Recorded data during a single power cycle. Representative (a) current, (b) voltage, (c) power, (d) junction temperature, and (e) case temperature in single power cycle.

theoretically enables high-temperature operation in SiC power module packaging due to its high melting point (961.8 °C [57]), its microstructure deteriorates significantly under power cycling at a junction temperature of 200 °C. This issue requires further investigation and resolution. In contrast, despite severe plastic deformation and cracking in the Al layer of the DBA substrate, the Ag–Al bond remained robust. This is an interesting point worthy of discussion. The bonding mechanism between them will be discussed in detail in the following sections.

B. Microstructure Evolution of SiC/ Sintered AgAl/DBA Structure During Power Cycling

To mitigate the microstructural degradation of the sintered Ag layer during power cycling, sintered AgAl composite pastes were specifically developed for DBA substrates, based on the unique nanoparticle emission phenomenon of Ag flakes. A systematic study was conducted to investigate the microstructural evolution of sintered AgAl/DBA joints during power cycling.

Fig. 7 presents the CT results of three different compositions of sintered AgAl/DBA joints after 10000 cycles. With 5 wt.% Al content (Fig. 7(a)), distinct crack lines were observed, but the crack density was lower than that of pure sintered Ag/DBA joint (Fig. 5(c)). At higher magnification (Fig. 7(a1)), faint crack lines were detected, indicating mild cracks. The average crack spacing was 113.8 μm (Figs. 7(a) and (a1)), significantly greater than that of the pure sintered Ag/DBA joint (71.6 μm, Fig. 5(c) and (c1)). This indicates that the crack density decreases with the addition of Al particles, suggesting the addition of Al effectively suppresses crack formation. With increasing Al content, crack lines became less sharp, further indicating reduced degradation of the sintered AgAl layer. At 15 wt.% Al content (Figs. 7(c) and (c1)), the average crack spacing was 154.1 μm. These results demonstrate that the addition of Al effectively inhibits the microstructural degradation of the sintered layer.

Fig. 8 presents SEM images of sintered AgAl/DBA joints with varying Al content after 10000 power cycles. By comparing Figs. 8(a)-(c), it is evident that the degradation of the sintered AgAl/DBA structure was effectively inhibited. This result is consistent with the CT results in Fig. 7. For the sintered layer, as the Al content increased, the microstructure evolved from localized collapse to only longitudinal cracks, and finally to a reduced crack density. Microstructural degradation in the sintered layer was effectively suppressed. For the DBA substrate, plastic deformation was also effectively inhibited, and crack formation was significantly reduced. When the Al content is 5 wt.%, the crack density in the DBA substrate is significantly reduced compared to the sintered Ag/DBA structure, with a corresponding crack

spacing of 110.2 μm. Moreover, the crack depth is also reduced. As the Al content increases further, the degree of degradation in the DBA substrate is further mitigated. Therefore, the addition of Al particles significantly improved the microstructural stability of the sintered AgAl/DBA structure.

For the high-magnification SEM images, since the interface between the sintered Ag and DBA substrate was systematically analyzed in Fig. 6, here we focus on the interface between the Ag and Al particles in the sintered layer. The high-magnification image of area 1 in Fig. 8(a) is shown in Fig. 8(a1), where Al particles are uniformly distributed in the sintered Ag layer. Fig. 8(a2) shows the high-magnification image of area 4 in Fig. 8(a1), indicating that after 10000 cycles of power cycling, Al particles and the sintered Ag remained well-bonded. Moreover, compared with the pure sintered Ag layer (Fig. 6(c1)), microstructural coarsening was inhibited, likely due to Al particles blocking Ag atom diffusion pathways. The high-magnification image of area 2 in Fig. 8(b) is shown in Fig. 8(b1), where a higher proportion of Al particles are uniformly distributed in the sintered Ag matrix. The corresponding high-magnification SEM image (Fig. 8(b2)) also indicates that the sintered necks of Ag and Al particles are well-bonded. Similar results can be observed for the sintered Ag15Al/DBA joint. In summary, the high-magnification SEM results indicate that after 10000 cycles, the sintered necks of Ag and Al particles remained tightly bonded at the micron scale in the sintered layer. Additionally, Al particle addition inhibits coarsening of the sintered Ag layer.

C. Real-Time Thermal Characteristics Monitoring During Power Cycling

Figs. 9(a)-(e) present the data recorded during a single power cycle. Fig. 9(a) shows the applied constant current, maintained for 2 seconds. At the initial stage of switching on, a peak is observed, which is called the surge spike phenomenon [58]. This is primarily caused by the physical characteristics of energy storage components in the circuit, especially capacitors and inductors, as well as the transient nature of the switching operation. This phenomenon is attributed to the design and construction of the power cycling apparatus and is an objectively existing behavior. Similar observations have also been reported in previous studies using the same testing equipment [39]. Fig. 9(b) presents the voltage profile, where a similar surge spike is observed. Additionally, during the 1-3 seconds (switch-on period), the voltage exhibits an upward trend. This occurs because power applications cause continuous temperature rise, increasing the resistance of the Pt heater wire. As a result, under constant current mode, the corresponding voltage increases. According to the results from Figs. 9(a) and (b), the real-time power (P), shown in Fig. 9(c), can be calculated using Equation (2). Figs. 9(d) and (e) display the monitored junction temperature and case temperature, respectively. Until now, the three critical data: junction temperature (T_j), case temperature (T_c), and power (P)—have been obtained. By applying Equation (1), the transient thermal resistance for a single cycle can be determined. During extended power cycling, transient thermal resistance is continuously monitored in real time.

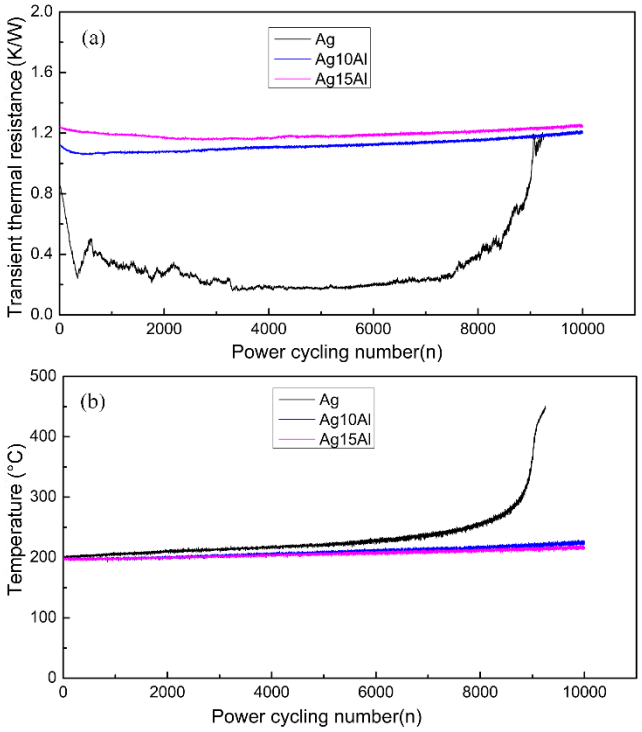

Fig. 10 The real-time thermal characteristics monitoring during power cycling. (a) Transient thermal resistance, (b) Transient maximum junction temperature during power cycling.

TABLE II
TRANSIENT THERMAL RESISTANCE

Paste	Initial (K/W)	End (K/W)	Increment
Ag	0.860	1.203	39.9%
Ag10Al	1.126	1.209	7.4%
Ag15Al	1.238	1.244	0.5%

TABLE III
MAXIMUM JUNCTION TEMPERATURE

Paste	Initial (°C)	End (°C)	Increment
Ag	200	446.0	123.0%
Ag10Al	200	224.3	12.2%
Ag15Al	200	215.2	7.6%

Here, three representative pastes (sintered Ag, Ag10Al, and Ag15Al) were selected, and the transient thermal resistance of their sintered mimicked SiC/DBA power modules during power cycling are shown in Fig. 10(a). The black curve represents the transient thermal resistance of the SiC/sintered Ag/DBA module. Initially, the transient thermal resistance of the SiC/sintered Ag/DBA power module was 0.860 K/W, as shown in Table 2. During the 0-3000 cycles, the transient thermal resistance exhibited a downward trend due to the settling effect of the TIM pad [59], the similar phenomenon was observed in previous studies [60]. Due to the significant CTE mismatch between the sintered Ag and the DBA substrate, noticeable plastic deformation occurred in the DBA substrate. Under the combined effects of temperature and pressure, this deformation enhanced the conformity between

the DBA substrate and the TIM, thereby resulting in a pronounced settling effect. The essential settling mechanism will be studied in the future, and the statistical number of samples will also increase. From 3000 to 7000 cycles, transient thermal resistance remained stable. However, after 7000 cycles, transient thermal resistance increased sharply. This increase was attributed to degradation of the sintered Ag layer and DBA substrate (Fig. 6), which reduced heat dissipation efficiency. By 9200 cycles, transient thermal resistance reached a level where heat from the heater chip could no longer be dissipated effectively, ultimately causing SiC heater chip failure. The SEM image of the failed heater chip is shown in Fig. S2. At this point, transient thermal resistance rose to 1.203 K/W, a 39.9% increase from its initial value. This increase exceeds the failure criterion for power devices (transient thermal resistance increase of 20%) [61], indicating that the SiC/sintered Ag/DBA structured power module had failed. These findings indicate that the SiC/Ag/DBA module exhibited poor reliability, and the excellent performance of the DBA substrate and sintered Ag was not fully realized.

The blue curve in Fig. 10(a) shows the transient thermal resistance monitoring results for the SiC/sintered Ag10Al/DBA power module during power cycling. Similar to the pure Ag sintered module, it initially exhibited a decrease in transient thermal resistance, followed by a slight increase. However, the increase was significantly lower than that of the pure Ag sintered module after long-term service. The initial transient thermal resistance of the SiC/sintered Ag10Al/DBA module was 1.126 K/W, higher than that of the SiC/sintered Ag/DBA module. This can be attributed to the higher thermal conductivity of pure Ag paste compared to Ag10Al paste. On one hand, the thermal conductivity of Al is lower than that of Ag [62]. On the other hand, with increasing Al content, the interfacial area between Ag and Al particles increases, which weakens the electron–phonon coupling effect in interfacial heat transfer [63]. However, after 10000 cycles, the transient thermal resistance increased to 1.209 K/W (as shown in Table 2), representing only a 7.4% increase from the initial stage, significantly lower than the 39.9% increase for the SiC/sintered Ag/DBA module. This result indicates that Al particle addition effectively enhances power module reliability.

The SiC/sintered Ag15Al/DBA power module (purple curve in Fig. 10(a)) also demonstrates good thermal stability during power cycling. Initially, the transient thermal resistance of the Ag15Al sintered SiC/DBA power module was 1.238 K/W, slightly higher than Ag10Al due to its higher Al content. After 10000 cycles, the transient thermal resistance of the SiC/sintered Ag15Al/DBA power module was 1.244 K/W (shown in Table 2), representing only a 0.5% increase from the initial stage. This demonstrates excellent transient thermal resistance stability. This result is also better than the reliability of the SiC/Pb5Sn/DBC structure [40], where the initial junction temperature is 200°C and the transient thermal resistance increases by 36% after 8800 cycles, indicating that device failure had occurred.

Fig. 10(b) shows the real-time monitoring results of the maximum junction temperature of the power module during the power cycling, with an initial value of 200°C. As the number of cycles increases, the junction temperature exhibits a continuous upward trend. This trend results from microstructural degradation, which reduces the module's heat dissipation capability. The summary of the junction temperature results is provided in Table 3. For the SiC/sintered Ag/DBA module (black curve), junction temperature gradually increases with cycling. From 0 to 7000 cycles, the junction temperature increases slowly. However, after 7000 cycles, the junction temperature rises sharply, indicating a significant decline in the module's heat dissipation capability. By 9200 cycles, the junction temperature reached 416°C, a 123.0% increase from its initial value. In contrast, for the SiC/sintered Ag10Al/DBA power module, after 10000 cycles, the junction temperature reached 224.3°C, representing a 12.2% increase from the initial value. This result is lower than that of the pure Ag sintered module, further indicating that the addition of Al particles effectively improves the module's reliability and reduces the junction temperature after long-term service. For SiC/sintered Ag15Al/DBA power module, after 10000 cycles, the junction temperature was 215.2°C, representing a 7.6% increase from the initial stage.

Therefore, monitoring of the transient thermal resistance and junction temperature during power cycling was successfully implemented. The results indicate that for the pure Ag sintered power module, both transient thermal resistance and junction temperature increased significantly during power cycling, primarily due to microstructural degradation. In contrast, the AgAl sintered power module exhibited excellent stability in both transient thermal resistance and junction temperature throughout the cycling process. In summary, the addition of Al particles can effectively improve power cycling reliability, and the improvement becomes more pronounced with increasing Al content.

D. Lifetime Assessment of Pure Ag and Ag10Al Sintered Power Modules

To evaluate the effect of sintered AgAl composite paste on power cycling lifetime, a representative Ag10Al paste was selected for long-term tests, and its performance was compared with that of a pure Ag-sintered power module. Fig. 11 shows the transient thermal resistance (Z_{th}) and junction temperature (T_j) curves of power modules sintered with pure Ag and Ag10Al during power cycling. According to AQG-324 [43], a 20% increase in transient thermal resistance is defined as the failure criterion. The initial transient thermal resistance of the pure Ag sintered module was 0.860 K/W. After 9043 cycles, the transient thermal resistance increased to 1.032 K/W, reaching 120% of the initial value, indicating the failure of the module. In contrast, for the power module with Ag10Al sintering, the initial transient thermal resistance was 0.946 K/W, and after 17675 cycles, the transient thermal resistance increased to 1.135 K/W, reaching 120% of its initial value. This indicates that the lifetime of the Ag10Al-sintered module reached 17675 cycles—approximately 1.95 times that of the pure Ag sintered module. These results clearly demonstrate that sintered Ag10Al paste significantly enhances the power cycling lifetime of power modules. As shown in Fig. 11(b), the junction temperature gradually increased with the number of cycles. However, the junction temperature rose sharply as

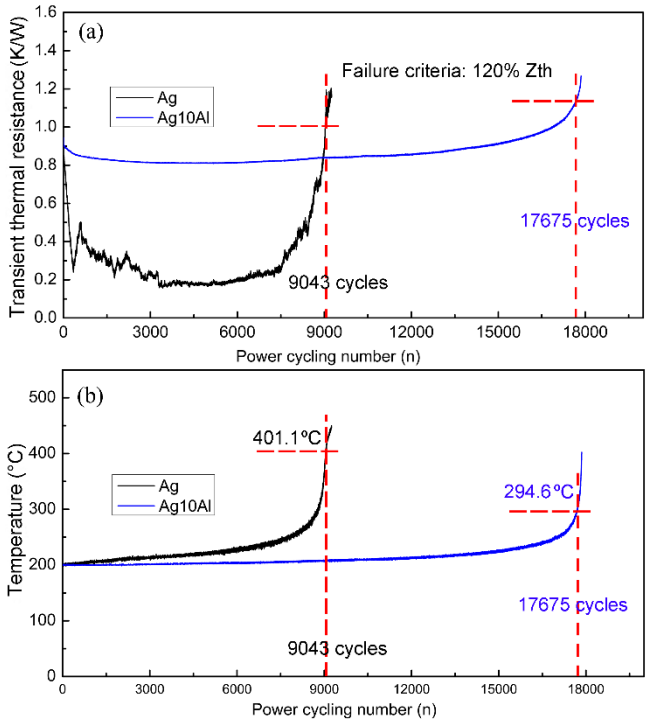

Fig. 11 Transient thermal resistance and junction temperature curves of pure Ag and Ag10Al sintered power modules during long terms power cycling test. (a) Transient thermal resistance, (b) Transient real-time maximum junction temperature.

failure approached. For the pure Ag-sintered module, the junction temperature reached 401.1°C after 9043 cycles, whereas the Ag10Al sintered module exhibited a junction temperature of 294.6°C after 17675 cycles. These findings indicate that under harsh power cycling conditions (temperature swing = 175°C, $T_{j,max}$ = 200°C), the Ag10Al sintered power module exhibited lower junction temperature rise and significantly extended lifetime.

E. Electrical Resistivity of Sintered AgAl

The die-attach layer serves not only as a thermal dissipation path but also as a critical component for electrical interconnection. Therefore, the electrical resistivity of the sintered AgAl composite paste was evaluated. Fig. 12 presents the resistivity of sintered AgAl composite pastes with varying Al content. The resistivity of pure sintered Ag is 5.63×10^{-8} Ω·m, as shown in Fig. 12. As the Al content increases, the resistivity of the sintered AgAl composite paste exhibits an upward trend. Specifically, the resistivity values for Ag5Al, Ag10Al, and Ag15Al are 8.96×10^{-8}, 9.19×10^{-8}, and 10.73×10^{-8} Ω·m, respectively.

Resistivity is an intrinsic property of conductive materials that characterizes the resistance to electric current per unit length and unit cross-sectional area. At the microscopic level, for pure metals (where the effects of impurities and defects can be neglected), resistivity primarily arises from electron scattering caused by lattice vibrations [64], which is temperature dependent. However, in real materials, the presence of impurities and defects disrupts the periodic potential field, leading to additional electron scattering. Generally, in metallic materials, the influence of impurities and defects on resistivity is the temperature independent but

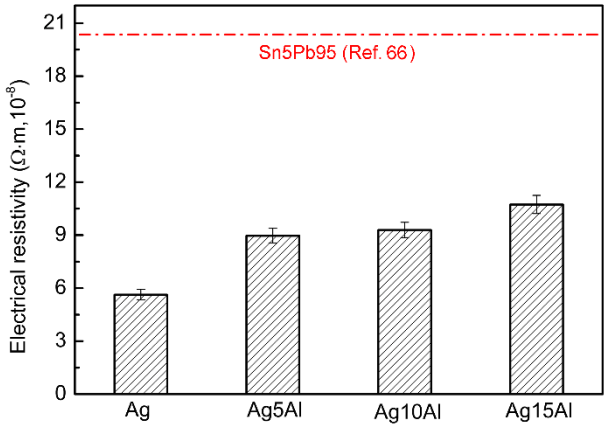

Fig. 12 The electrical resistivity of sintered AgAl composite pastes with varying Al content.

proportional to their concentration [65]. Therefore, any factor that affects electron scattering will alter the resistivity of the material. The introduction of Al particles disrupts the regular electron scattering in pure sintered Ag, thereby increasing increased resistivity. Nevertheless, even with 15 wt.% Al, the resistivity of sintered Ag15Al remains lower than that of Sn5Pb95 solder [66].

IV. Discussion

The above analysis systematically elucidates the microstructural degradation behavior in the SiC/ sintered Ag /DBA structure and proposes the SiC/sintered AgAl/DBA structure as an improvement to mitigate the degradation. To gain insight into the improvement mechanism of degradation behavior of power module, in this section, we will explore it from two aspects: macroscopic CTE and microscopic interface between Ag and Al. The Ag–Al interface includes two types: the interface between sintered Ag and the Al layer of the DBA substrate, and the interface between Ag and Al particles within the sintered AgAl layer.

A. CTE of Sintered AgAl Composite Pastes

Power cycling primarily evaluates the degradation behavior of packaging materials with different CTEs under cyclic junction temperature fluctuations. Therefore, CTE mismatch is a key factor limiting the lifespan of power devices [34]. For the sintered Ag layer, the bonding with the upper SiC is through sputtered Ag, forming a homogeneous material interface. In contrast, bonding with the DBA substrate involves heterogeneous materials (Ag and Al), leading to inconsistent bonding strengths compared to upper interface. As evidenced by the microstructural evolution results in Figs. 6 and 7, the Al substrate in the DBA undergoes significant plastic deformation during power cycling, and longitudinal crack propagation in the sintered layer also initiates from the bottom due to the severe deformation of DBA substrate. Previous studies have demonstrated that stress at the bottom of the sintered Ag layer is greater than at the top [67]. Therefore, reducing the CTE difference between the DBA substrate and the sintered layer is essential to suppress microstructural degradation.

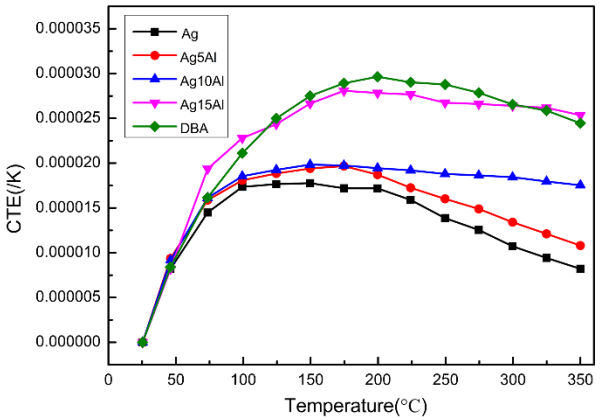

Fig. 13 CTE results of the DBA substrate, sintered Ag, and sintered AgAl with various Al particles addition.

Fig. 13 presents the CTE results of the DBA substrate, sintered Ag, and sintered AgAl with varying Al content over the temperature range of 25-350°C. For the DBA substrate, the CTE initially increases with temperature, peaking at 29.6 × 10^{-6}/K at 200°C, followed by a slight decrease due to the softening of Al in the DBA substrate [68]. For pure sintered Ag, the CTE shows a similar trend. it reaches 17.2 × 10^{-6}/K at 200°C, resulting in a CTE difference of 12.4 × 10^{-6}/K compared to the DBA substrate. This mismatch leads to plastic deformation and cracking in the sintered Ag/DBA structure, as shown in Fig. 6(c). As the temperature increases, CTE decreases due to shrinkage from further sintering of porous Ag, suggesting potential instability at elevated temperatures.

With 5 wt.% Al added (Ag5Al), the CTE trend with temperature is similar but with higher values compared to pure sintered Ag. At 200°C, it reaches 18.7 × 10^{-6}/K. For 10 wt.% Al (Ag10Al), the CTE values from 25-200°C are almost identical to Ag5Al, but the decrease in CTE above 200°C is less pronounced, demonstrating better high-temperature stability. When 15 wt.% Al particles are added (Ag15Al), the material exhibits both high CTE values and high-temperature stability, with a CTE value of 27.8 × 10^{-6}/K at 200°C, and a minimal CTE difference of only 1.8 × 10^{-6}/K compared to the DBA substrate. Moreover, from 25–200°C, the CTE mismatch between Ag15Al and the DBA substrate remains minimal.

These results indicate that the addition of Al particles effectively reduces the CTE mismatch between the sintered layer and the DBA substrate. This explains why the degradation of the microstructure is significantly improved with the addition of Al particles in Figs. 7 and 8. Additionally, due to the smaller CTE mismatch, the lifetime of AgAl sintered power module is almost twice that of pure Ag, as shown in Fig. 11.

B. The Interface Between Sintered Ag and DBA Substrate During Power Cycling

In addition to the CTE of the sintered layer, it is crucial to investigate the interfacial bonding mechanisms at the nanoscale or atomic level during power cycling. Next, the interface at the initial stage and after power cycling are discussed respectively.

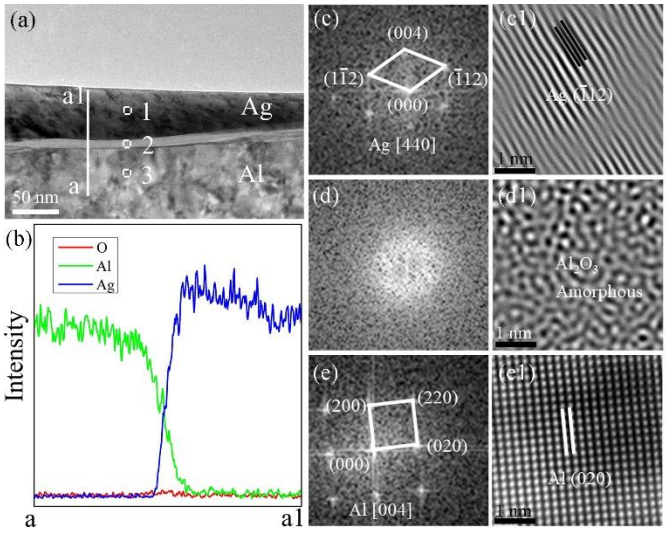

Fig. 14 The sintered Ag/DBA substrate interface at the initial stage. (a) TEM image. (b) EDS along a-a1 line in Fig. 14(a). (c) FFT and (c1) IFFT images of area 1 in Fig. 14(a); (d) FFT and (d1) IFFT images of area 2 in Fig. 14(a); (e) FFT and (e1) IFFT images of area 3 in Fig. 14(a), respectively.

(1) The interface between sintered Ag and DBA substrate at the initial stage

Fig. 14(a) shows the TEM image of the sintered Ag/DBA substrate at initial state, revealing a typical sandwich structure. Fig. 14(b) presents EDS results along the a–a1 line in Fig. 14(a). Almost no Al is detected on the Ag side, indicating that diffusion does not occur at the initial stage. To determine the phases present in interface regions, fast Fourier Transform (FFT) and inverse fast Fourier Transform (IFFT) were conducted on areas 1, 2, and 3 in Fig. 14(a), respectively.

The FFT image of area 1 in Fig. 14(a), shown in Fig. 14(c), is indexed to the Ag (1$\bar{1}$2), ($\bar{1}$12), and (004) planes, with a zone axis of [440]. The corresponding IFFT image of the ($\bar{1}$12) plane, shown in Fig. 14(c1), clearly displays lattice fringes. Similarly, the FFT image of area 3 in Fig. 14(a), shown in Fig. 14(e), is indexed to the Al (200), (020), and (220) planes, with a zone axis of [004]. The corresponding IFFT image, shown in Fig. 14(e1), reveals periodically arranged Al atoms. The parallel lines represent the Al (020) plane with a spacing of 0.202 nm. In contrast to Figs. 14(c) and (e), the FFT image of area 2 in Fig. 14(a), shown in Fig. 14(d), does not display periodic diffraction spots but rather an amorphous ring. The corresponding IFFT image further confirms the amorphous structure. Based on the natural oxidation tendency of Al and previous studies [32,69], area 2 is identified as amorphous Al_2O_3. In summary, the Al_2O_3 layer on the surface of the DBA substrate exists in an amorphous state. The bonding between the sintered Ag and the DBA substrate essentially occurs through the interconnection between Ag and the amorphous Al_2O_3. Due to the presence of the Al_2O_3 barrier layer, there is no direct contact between Ag and Al, and no mutual diffusion occurs. It is consistent with the results of EDS (Fig. 14(b)). These findings clarify the fundamental interconnection mechanism between sintered Ag and the DBA substrate.

(2) Sintered Ag/DBA interface after power cycling

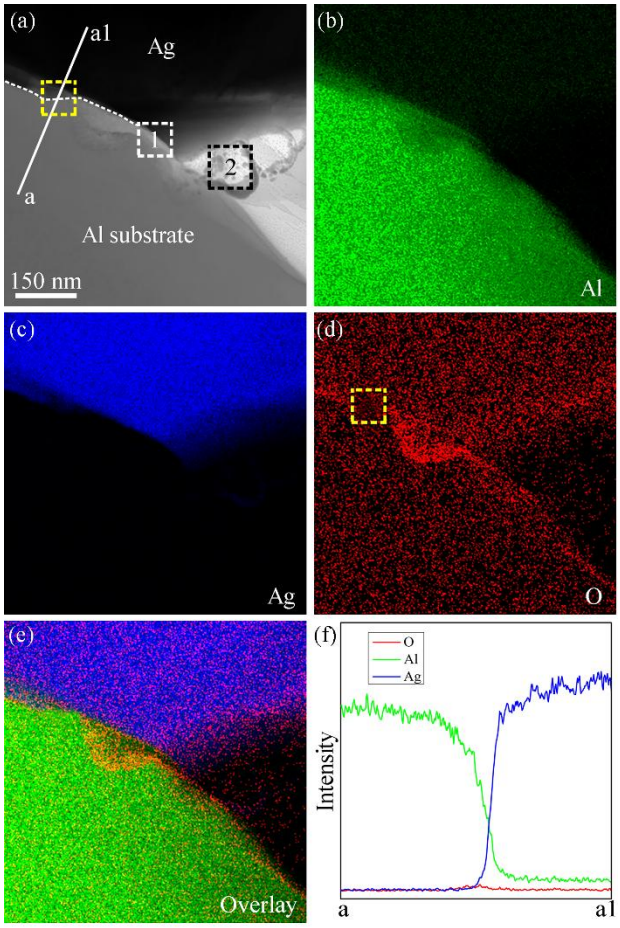

Fig. 15 TEM and EDS images of the sintered Ag/DBA substrate after power cycling. (a) TEM image. EDS maps of (b) Al, (c) Ag, (d) O, and (e) their overlay. (f) EDS along a-a1 line in Fig. 15(a).

Fig. 15(a) shows the TEM image of the sintered Ag/DBA substrate after power cycling. Unlike the flat interface observed at the initial stage (Fig. 14(a)), the interface between Ag and Al becomes tortuous after power cycling (Fig. 15(a)). The interface is marked with dotted curves. EDS results [Figs. 15(b)–(e)] indicate that the black region in the upper right corresponds to sintered Ag, while the gray region in the lower left corresponds to Al in the DBA substrate. Fig. 15(b) shows the EDS map for Al element, indicating the presence of Al element not only in the Al area but also in the Ag region. This suggests that Al has diffused into the sintered Ag layer after power cycling. The EDS along a-a1 line in Fig. 15(a) (shown in Fig. 15(f)) further confirms the diffusion of Al into the sintered Ag layer. While the DBA substrate at the initial state is covered with a natural Al_2O_3 thin film, acting as a diffusion barrier. The natural Al_2O_3 film is attributed to the oxidation of Al in the DBA substrate at room temperature. Therefore, this raises the question: how does Al diffuse through the Al_2O_3 layer into the Ag layer?

During power cycling, the sintered Ag/DBA structure undergoes alternating stress and strain, causing deformation and even cracking of the DBA substrate, as previously shown in Fig. 6. This can lead to cracking and local detachment of the brittle Al_2O_3 layer, exposing fresh, oxide-free Al surfaces. Simultaneously, the continuous alternating deformation cause some sintered Ag to be squeezed into these fresh Al areas,

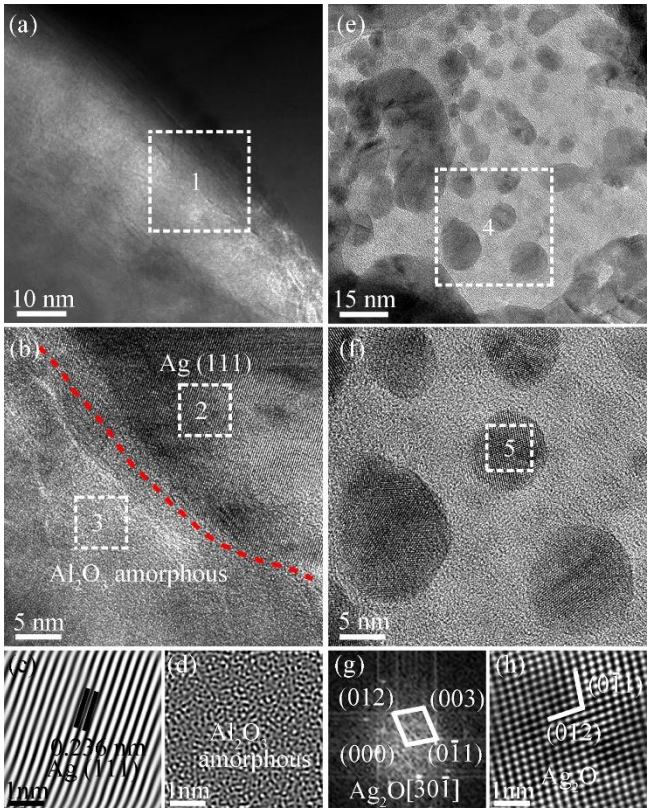

Fig. 16 HRTEM image of Ag/DBA interface. (a) High-magnification view of area 1 in Fig. 15(a). (b) HRTEM image of area 1 in Fig. 16(a). IFFT images of (c) areas 2 and (d) area 3 in Fig. 16(b), respectively. (e) High-magnification view of area 2 in Fig. 15(a). (f) HRTEM image of area 4 in Fig. 16(e). (g) FFT and (h) IFFT images of area 5 in Fig. 16(f).

forming direct contact between Al and Ag. Given the crystallographic information of Al and Ag [70,71], both Al and Ag belong a face-centered cubic (fcc) structure and have similar lattice constants—0.40494 nm for Al and 0.40862 nm for Ag. Therefore, during power cycling at elevated temperatures (T_j = 200°C), diffusion readily occurs.

In addition, Fig. 15(d) shows the EDS map for O element, revealing intermittent high-concentration signals at the interface. This indicates that the Al_2O_3 layer is discontinuous. In the yellow dashed box area of Fig. 15(d), the O signal is weaker than in other interfacial regions, representing the shedding of the Al_2O_3 layer due to plastic deformation. The corresponding region in Fig. 15(a), marked with a yellow dashed box, also indicated a deformation transition zone. This suggests that the Al_2O_3 layer tends to peel off in deformation transition zones, creating diffusion pathways for Ag and Al.

The above results discussed the shedding of Al_2O_3 layer in the deformed area of DBA substrate, which leads to the occurrence of diffusion. However, for the non-peeling area of Al_2O_3 layer, what is the interface bonding mechanism? Here, we selected a representative area, labeled area 1 in Fig. 15(a), for further investigation. The magnified image of area 1 (marked with a dotted frame) in Fig. 15(a) is shown in Fig. 16(a). In Fig. 16(a), a distinct interface line is difficult to identify. HRTEM observation was conducted in this area with notable contrast differences, as shown in Fig. 16(b). Clear lattice fringes are observed in the upper right of the red line [Fig. 16(b)], while no periodic fringes appear on the lower left.

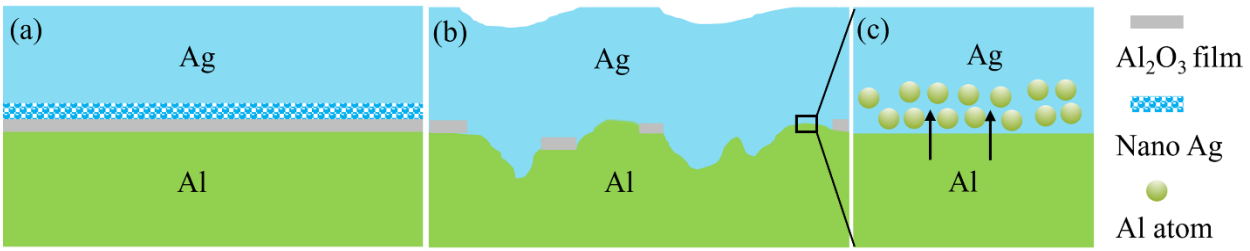

Fig. 17. The schematic diagram of the interface evolution between sintered Ag and the DBA substrate. (a) Initial stage. (b) After power cycling. (c) Al atoms diffuse into Ag.

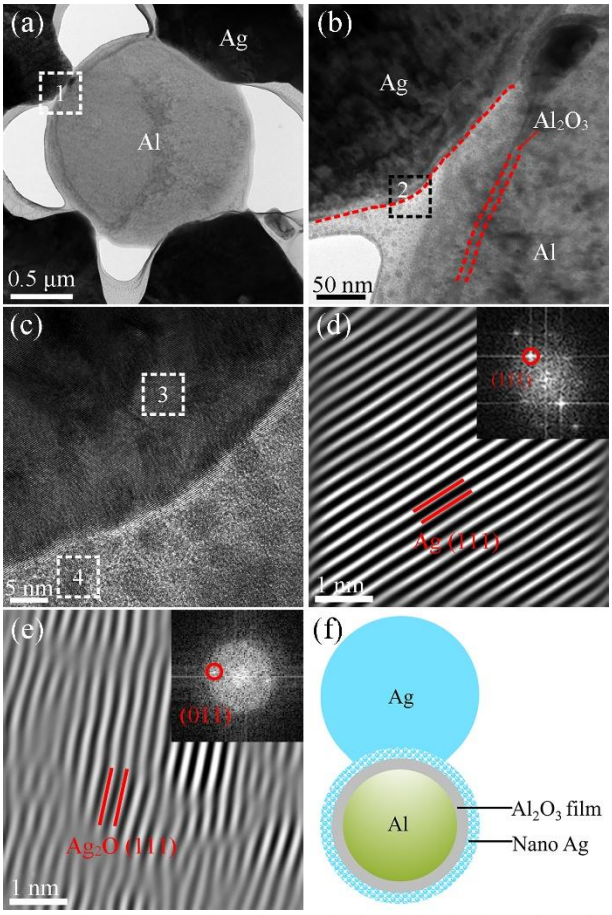

Fig. 18 Interface between sintered Ag and Al particles in sintered AgAl layer after 10000 power cycles. (a) TEM image of interface between Ag and Al particle. (b) The high-magnification view of area 1 in Fig. 18(a). (c) HRTEM image of area 2 in Fig. 18(b). IFFT images of (d) areas 3 and (e) area 4 in Fig. 18(c), respectively. (f) Schematic illustration of the bonding mechanism between Ag and Al particle.

To clarify this observation, IFFT analysis was performed. The IFFT results for areas 2 and 3 in Fig. 16(b) are shown in Figs. 16(c) and (d), respectively. Fig. 16(c) reveals clear lattice fringes with a spacing of 0.236 nm, indexed as the Ag (111) plane. While Fig. 16(d) exhibits an amorphous atomic distribution, indicating the presence of amorphous Al_2O_3. These results suggest that, in the non-peeling regions of Al_2O_3, the bonding mechanism remains the connection between Ag and Al_2O_3. However, unlike the clear interface line observed at the initial stage (Fig. 14), the interface between Ag and Al_2O_3 becomes blurred after power cycling.

Additionally, nanoparticles were observed in area 2 of Fig. 15(a). The high-magnification TEM image in Fig. 16(e) shows nanoparticles with an average size of 6.5 nm. The HRTEM image of area 4 in Fig. 16(e) is shown in Fig. 16(f). The FFT image of area 5 in Fig.16(f) is shown in Fig. 16(g), which can be indexed as the Ag_2O (012), $(0\bar{1}1)$, and (003) planes with a zone axis of $[30\bar{1}]$. The corresponding IFFT result is shown in Fig. 16(h). The results indicate that these ultrafine nanoparticles are Ag_2O. This is because of the ultrafine nano-Ag oxidized in the air, which is consistent with the result in Fig. 4. The difference is that Fig. 4 showed the ultrafine Ag nanoparticles were jetted in the initial stage. Therefore, the result in Fig. 16 (e) shows that the sintering Ag layer still produces new ultrafine Ag nanoparticles during the power cycle, resulting in re-sintering [38].

In summary, Fig. 17 shows the schematic diagram of the interface evolution between sintered Ag and the DBA substrate during the bonding and power cycling processes. In the bonding process (Fig. 17(a)), the unique nanoparticle ejection phenomenon of the micron sized Ag flakes enables in-situ surface modification of the DBA substrate, resulting in direct bonding between the sintered Ag and the DBA substrate. During the subsequent power cycling (Fig. 17(b)), under continuous alternating loads, the Al_2O_3 layer on the DBA surface undergoes localized cracking and detachment due to its inherent brittleness, leading to direct contact between Al and Ag. At elevated temperature (T_j = 200°C), Al atoms diffuse into the Ag, as shown in Fig. 17(c), forming a metallurgical bond. This bonding mechanism ensures reliable connection between micro-sized sintered Ag and the DBA substrate both initially and during power cycling.

C. The Interface Between Sintered Ag and Al Particles in Sintered AgAl Layer

Fig. 18(a) shows the TEM image of the sintered AgAl layer after 10000 power cycles, highlighting the interface between Ag and Al. The gray spherical particle in the center is Al particle, surrounded by the black sintered Ag. It is evident that the sintering neck of Ag is well bonded with the Al particle. Moreover, no cracks or significant plastic deformation are observed in the Al particle. This is likely due to the stress absorption by the pores within the porous structure during the power cycling [72]. The high-magnification view of area 1 from Fig. 18(a) is shown in Fig. 18(b). The lower right corner represents Al, covered by an Al_2O_3 layer (marked with dotted curves). The thickness of the Al_2O_3 layer is approximately 10 nm. A bright region containing numerous ultrafine nanoparticles exists between the Al_2O_3 layer and the sintered Ag. The HRTEM image of area 2 of Fig. 18(b) is depicted in Fig. 18(c). The IFFT images of areas 3 and 4 in Fig. 18(c) are

shown in Figs. 18(d) and (e), respectively, with corresponding FFT images inset in the upper right corners. The results indicate that the nanoparticles in Fig. 18(c) are Ag_2O, formed due to the oxidation of Ag nanoparticles during sintering and power cycling, similar result was reported in [38]. These Ag nanoparticles originate from the ultrafine nanoparticle ejection phenomenon of micron sized Ag flakes. Therefore, the bonding between micron-sized sintered Ag and Al particles is essentially enabled by the ultrafine Ag nanoparticles. The schematic illustration of the bonding mechanism between Ag and Al in the sintered AgAl layer is shown in Fig. 18(f). Al particles are naturally covered by an Al_2O_3 layer, which has been verified by previous studies [38,73]. And the ultrafine nanoparticle ejection phenomenon of Ag flakes allows Ag nanoparticles to cover the surface of Al_2O_3, thereby achieving in-situ surface modification of Al particles. Consequently, the bonding between micron-sized Ag flakes and nanometer-sized Ag particles is readily achieved.

In summary, the mechanism for improving the degradation of the microstructure has been elucidated from both macroscopic and microscopic perspectives. At the macroscopic level, adding appropriate Al particles reduces the CTE mismatch between the sintered layer and the DBA substrate. At the microscopic level, the direct bonding of micron-sized sintered Ag with the DBA substrate and Al particles is attributed to the nanoparticle ejection phenomenon of micron-sized Ag flakes, enabling in-situ surface modification of the DBA substrate. During subsequent power cycling, plastic deformation of Al in the DBA substrate causes partial cracking of the Al_2O_3 layer, thereby facilitating the diffusion of Al into the sintered Ag layer and achieving a metallurgical bond.

V. Conclusion

1. Based on the robust bonding between Ag and Al, the SiC/sintered AgAl/DBA structure was proposed. Compared with the SiC/sintered Ag/DBA structure, it exhibited superior microstructural and transient thermal resistance stability during power cycling. This offers a new approach for designing high-reliability SiC power modules.
2. During power cycling at a junction temperature of 200°C, the sintered Ag layer experienced significant degradation. To suppress the microstructural degradation of the sintered Ag layer, sintered AgAl composite pastes specifically designed for DBA substrates were developed. The degradation of the sintered SiC/sintered AgAl/DBA structure was effectively suppressed. The result is attributed to reduced CTE mismatch between the sintered AgAl layer and the DBA substrate, as well as robust bonding between sintered Ag and Al.
3. The unique nanoparticle ejection of the micron-sized Ag flakes enables in-situ surface modification of the DBA substrate, resulting in direct bonding between the sintered Ag and the DBA substrate. During subsequent power cycling, under continuous alternating loads, the Al_2O_3 layer on the DBA surface undergoes localized cracking and detachment due to its inherent brittleness, leading to direct contact between Al and Ag. At elevated temperatures (T_j = 200°C), Al atoms diffuse into the Ag, forming a metallurgical bond.
4. Based on the self-developed instrument, real-time monitoring of transient thermal resistance and junction temperature during power cycling was achieved. For the SiC/sintered Ag/DBA structured power module, after 9200 power cycles, the transient thermal resistance and junction temperature increased by 39.9% and 123.0%, respectively, compared to the initial stage. In contrast, for the newly developed SiC/sintered Ag15Al/DBA structured power module, the transient thermal resistance and junction temperature after 10000 cycles only increased by 0.5% and 7.6%, respectively, which is significantly lower than that of the SiC/sintered Ag/DBA structured power module. A highly reliable SiC power module structure has been successfully developed.

References

[1] X. Li, Y. Chen, H. Chen, R. Paul, X. Song, and H. A. Mantooth, "A 10 kV SiC MOSFET Power Module with Optimized System Interface and Electric Field Distribution," IEEE Trans Power Electron, vol. 39, no. 8, pp. 9540–9553, 2024, doi: 10.1109/TPEL.2024.3392273.

[2] X. Chen, Q. Wang, X. Huang, M. Awais, A. Paramane, and N. Ren, "Investigation of Electrical and Thermal Properties of Epoxy Resin/Silicon Carbide Whisker Composites for Electronic Packaging Materials," IEEE Trans Components, Packag Manuf Technol, vol. 12, no. 7, pp. 1109–1121, 2022, doi: 10.1109/TCPMT.2022.3178741.

[3] D. Lu, X. Wang, H. Pan, X. Zheng, M. Li, and H. Ji, "Low-Temperature Direct Bonding of Sputtered Nanocrystalline Ag Film for Power Electronic Packaging: Bonding Mechanism, Thermal Characteristics, and Reliability," IEEE Trans Power Electron, vol. 39, no. 5, pp. 6040–6051, 2024, doi: 10.1109/TPEL.2024.3368666.

[4] X. Yuan, I. Laird, and S. Walder, "Opportunities, Challenges, and Potential Solutions in the Application of Fast-Switching SiC Power Devices and Converters," IEEE Trans Power Electron, vol. 36, no. 4, pp. 3925–3945, 2021, doi: 10.1109/TPEL.2020.3024862.

[5] D. Zhao, C. Zhao, Z. Xiu, and J. Yan, "Understanding the formation mechanism of SiC/Al joints by U-TLP bonding with the inactive Zn interlayer," J Mater Sci Technol, vol. 201, pp. 236–249, 2024, doi: 10.1016/j.jmst.2024.02.036.

[6] Y. Zuo, C. Zhao, A. Robador, M. Wickham, and S. H. Mannan, "Quasi-in-situ observation of the grain growth and grain boundary movement in sintered Cu nanoparticle interconnects," Acta Mater, vol. 236, p. 118135, 2022, doi: 10.1016/j.actamat.2022.118135.

[7] G. Chang, D. An, E. Deng, X. Li, H. Luo, and Y. Huang, "Research on the Key Processes of Large-Area Silver Sintering for SiC Power Modules," IEEE Trans Components, Packag Manuf Technol, vol. 15, no. 2, pp. 410–420, 2025, doi: 10.1109/TCPMT.2025.3531127.

[8] X. Liu, H. Tatsumi, J. Wang, Z. Jin, Z. Chen, and H. Nishikawa, "Analysis of microstructures and fractures in Ag–In transient liquid phase bonded joints," Mater Sci Eng A, vol. 892, no. December 2023, 2024, doi: 10.1016/j.msea.2023.146045.

[9] B. Zhang, S. Zhang, X. Lu, L. Han, and Y. H. Mei, "Reliability Improvement of Low-Temperature Sintered Nano-Silver as Die Attachment by Porosity Optimization," IEEE Trans Components, Packag Manuf Technol, vol. 13, no. 8, pp. 1209–1217, 2023, doi: 10.1109/TCPMT.2023.3299291.

[10] J. Son, D. Y. Yu, Y. C. Kim, S. Il Kim, D. Byun, and J. Bang, "Thermal reliability of Cu sintering joints for high-temperature die attach," Microelectron Reliab, vol. 147, no. March, p. 115002, 2023, doi: 10.1016/j.microrel.2023.115002.

[11] J. He et al., "Microstructure evolution and deformation behavior of Au–20Sn eutectic alloy during hot rolling process," J Alloys Compd, vol. 831, p. 154824, 2020, doi: 10.1016/j.jallcom.2020.154824.

[12] Y. Wu, G. Zou, S. Wang, W. Guo, H. Zhang, and L. Liu, "Interfacial bonding mechanisms of sintered Cu nanoparticles on different metallization surfaces," Surfaces and Interfaces, vol. 46, no. February, p. 104173, 2024, doi: 10.1016/j.surfin.2024.104173.

[13] L. Du et al., "Microstructural and mechanical anisotropy in pressure-assisted sintered copper nanoparticles," Acta Mater, vol. 287, no. February, p. 120772, 2025, doi: 10.1016/j.actamat.2025.120772.

[14] J. Xin et al., "High performance Cu sintering joint for power devices enabled by in-situ generation of Cu particles with multi-level hierarchical structures," J Mater Process Technol, vol. 329, no. May, pp. 1–11, 2024, doi: 10.1016/j.jmatprotec.2024.118435.

[15] T. F. Chen and K. S. Siow, "Comparing the mechanical and thermal-electrical properties of sintered copper (Cu) and sintered silver (Ag) joints," J Alloys Compd, vol. 866, p. 158783, 2021, doi: 10.1016/j.jallcom.2021.158783.

[16] J. Fan, G. Li, K. Rajavel, P. Zhu, R. Sun, and C. P. Wong, "Synergistic size and shape effect of dendritic silver nanostructures for low-temperature sintering of paste as die attach materials," J Mater Sci Mater Electron, vol. 32, no. 1, pp. 323–336, 2021, doi: 10.1007/s10854-020-04783-9.

[17] U. Ulusoy, "A Review of Particle Shape Effects on Material Properties for Various Engineering Applications: From Macro to Nanoscale," Minerals, vol. 13, no. 1, 2023, doi: 10.3390/min13010091.

[18] K. S. Siow, "Mechanical properties of nano-silver joints as die attach materials," J Alloys Compd, vol. 514, pp. 6–19, 2012, doi: 10.1016/j.jallcom.2011.10.092.

[19] S. A. Paknejad, G. Dumas, G. West, G. Lewis, and S. H. Mannan, "Microstructure evolution during 300°C storage of sintered Ag nanoparticles on Ag and Au substrates," J Alloys Compd, vol. 617, pp. 994–1001, 2014, doi: 10.1016/j.jallcom.2014.08.062.

[20] Z. Zhang, C. Chen, A. Suetake, M. C. Hsieh, A. Iwaki, and K. Suganuma, "Pressureless and low-temperature sinter-joining on bare Si, SiC and GaN by a Ag flake paste," Scr Mater, vol. 198, p. 113833, 2021, doi: 10.1016/j.scriptamat.2021.113833.

[21] C. Chen and K. Suganuma, "Large-scale ceramic–metal joining by nano-grained Ag particles paste sintering in low-temperature pressure-less conditions," Scr Mater, vol. 195, 2021, doi: 10.1016/j.scriptamat.2021.113747.

[22] Z. Zhang et al., "Low-temperature and pressureless sinter joining of Cu with micron/submicron Ag particle paste in air," J Alloys Compd, vol. 780, pp. 435–442, 2019, doi: 10.1016/j.jallcom.2018.11.251.

[23] L. Xu, M. Wang, Y. Zhou, Z. Qian, and S. Liu, "An optimal structural design to improve the reliability of Al2O3-DBC substrates under thermal cycling," Microelectron Reliab, vol. 56, pp. 101–108, 2016, doi: 10.1016/j.microrel.2015.11.013.

[24] L. Xu, S. Liu, M. Wang, and S. Zhou, "Crack initiation and propagation mechanism of Al2O3-DBC substrate during thermal cycling test," Eng Fail Anal, vol. 116, no. April, p. 104720, 2020, doi: 10.1016/j.engfailanal.2020.104720.

[25] S. T. Chua and K. S. Siow, "Microstructural studies and bonding strength of pressureless sintered nano-silver joints on silver, direct bond copper (DBC) and copper substrates aged at 300 °C," J Alloys Compd, vol. 687, pp. 486–498, 2016, doi: 10.1016/j.jallcom.2016.06.132.

[26] Y. Liu et al., "Development of crack-less and deformation-resistant electroplated Ni/electroless Ni/Pt/Ag metallization layers for Ag-sintered joint during a harsh thermal shock," Mater Des, vol. 224, p. 111389, 2022, doi: 10.1016/j.matdes.2022.111389.

[27] Q. Xu, Y. Mei, X. Li, and G. Q. Lu, "Correlation between interfacial microstructure and bonding strength of sintered nanosilver on ENIG and electroplated Ni/Au direct-bond-copper (DBC) substrates," J Alloys Compd, vol. 675, pp. 317–324, 2016, doi: 10.1016/j.jallcom.2016.03.133.

[28] C. Chen, N. Sato, T. Ogushi, S. Nagao, and K. Suganuma, "Thermal conductivity and interface thermal resistance evaluation of DBC/DBA in power die attach modules," PCIM Eur Conf Proc, no. May, pp. 879–883, 2019.

[29] C. Chen et al., "Interface reaction and evolution of micron-sized Ag particles paste joining on electroless Ni-/Pd-/Au-finished DBA and DBC substrates during extreme thermal shock test," J Alloys Compd, vol. 862, p. 158596, 2021, doi: 10.1016/j.jallcom.2021.158596.

[30] D. P. Hamilton, S. Riches, M. Meisser, L. Mills, and P. Mawby, "High temperature thermal cycling performance of DBA, AMB and thick film power module substrates," CIPS 2016 - 9th Int Conf Integr Power Electron Syst, pp. 1–5, 2019.

[31] X. Si, C. Li, Y. Bo, J. Qi, J. Feng, and J. Cao, "The role of Al diffusion behavior in the process of forming a super-reliable Al2O3 protective layer during reactive air aluminization," Appl Surf Sci, vol. 518, no. February, p. 146242, 2020, doi: 10.1016/j.apsusc.2020.146242.

[32] C. Chen et al., "Interface-Mechanical and Thermal Characteristics of Ag Sinter Joining on Bare DBA Substrate during Aging, Thermal Shock and 1200 W/cm2Power Cycling Tests," IEEE Trans Power Electron, vol. 37, no. 6, pp. 6647–6659, 2022, doi: 10.1109/TPEL.2022.3142286.

[33] Q. Jia et al., "Sintering Mechanism of a Supersaturated Ag-Cu Nanoalloy Film for Power Electronic Packaging," ACS Appl Mater Interfaces, vol. 12, no. 14, pp. 16743–16752, 2020, doi: 10.1021/acsami.9b20731.

[34] C. C. Lee, K. S. Kao, and Y. C. Huang, "Experimental and Simulated Verification of Power Cycling Reliability for Thin and Low Warpage Power Modules," IEEE Trans Power Electron, vol. PP, pp. 1–12, 2024, doi: 10.1109/TPEL.2024.3414829.

[35] H. Zhang, C. Chen, S. Nagao, and K. Suganuma, "Thermal Fatigue Behavior of Silicon-Carbide-Doped Silver Microflake Sinter Joints for Die Attachment in Silicon/Silicon Carbide Power Devices," J Electron Mater, vol. 46, no. 2, pp. 1055–1060, 2017, doi: 10.1007/s11664-016-5069-1.

[36] F. Huo, Z. Jin, D. Le Han, J. Li, K. Zhang, and H. Nishikawa, "Novel interface regulation of Sn1.0Ag0.5Cu composite solders reinforced with modified ZrO2: Microstructure and mechanical properties," J Mater Sci Technol, vol. 125, pp. 157–170, 2022, doi: 10.1016/j.jmst.2022.01.040.

[37] Z. Wen, W. Liu, C. Hang, R. An, and Y. Tian, "Atomic insights into the sintering behaviour of Ag–Cu solid solution nanoparticles on Ag substrate," J Mater Res Technol, vol. 33, no. November, pp. 9123–9134, 2024, doi: 10.1016/j.jmrt.2024.11.241.

[38] F. Huo et al., "Interface regulation of micro-sized sintered Ag-10Al composite based on in-situ surface modification and enhanced microstructure stability in power electronic packaging," Mater Des, vol. 240, no. November 2023, p. 112863, 2024, doi: 10.1016/j.matdes.2024.112863.

[39] D. Kim, Y. Yamamoto, S. Nagao, N. Wakasugi, C. Chen, and K. Suganuma, "Measurement of heat dissipation and thermal-stability of power modules on DBC substrates with various ceramics by SiC Micro-heater chip system and ag sinter joining," Micromachines, vol. 10, no. 11, pp. 1–11, 2019, doi: 10.3390/mi10110745.

[40] D. Kim et al., "Online thermal resistance and Reliability Characteristic Monitoring of Power Modules with Ag Sinter Joining and Pb, Pb-Free Solders during Power Cycling Test by SiC TEG Chip," IEEE Trans Power Electron, vol. 36, no. 5, pp. 4977–4990, 2021, doi: 10.1109/TPEL.2020.3031670.

[41] W. Chen, P. Wang, Q. Cui, Z. Qiang, L. Qiao, and Q. Li, "Effect of titanium adhesion layer on the thermal stability of platinum films during vacuum high temperature treatment," Vacuum, vol. 226, no. May, p. 113295, 2024, doi: 10.1016/j.vacuum.2024.113295.

[42] G. Frost and L. Ladani, "Development of High-Temperature-Resistant Seed Layer for Electrodeposition of Copper for Microelectronic Applications," J Electron Mater, vol. 49, no. 2, pp. 1387–1395, 2020, doi: 10.1007/s11664-019-07826-y.

[43] D. Kim et al., "Power cycling tests under driving ΔTj = 125 °C on the Cu clip bonded EV power module," Microelectron Reliab, vol. 138, no. July, p. 114652, 2022, doi: 10.1016/j.microrel.2022.114652.

[44] J. D. James, J. A. Spittle, S. G. R. Brown, and R. W. Evans, "A review of measurement techniques for the thermal expansion coefficient of metals and alloys at elevated temperatures," Meas Sci Technol, vol. 12, no. 3, pp. 1–15, 2001, doi: 10.1088/0957-0233/12/3/201.

[45] C. Chen et al., "Low temperature low pressure solid-state porous Ag bonding for large area and its high-reliability design in die-attached power modules," Ceram Int, vol. 45, no. 7, pp. 9573–9579, 2019, doi: 10.1016/j.ceramint.2018.10.046.

[46] F. Huo et al., "Microstructure characteristics for improved thermal shock reliability of sintered Ag[sbnd]Al paste in SiC power module," Mater Charact, vol. 217, no. September, p. 114360, 2024, doi: 10.1016/j.matchar.2024.114360.

[47] Y. Liu et al., "Development of Ag@Si composite sinter joining with ultra-high resistance to thermal shock test for SiC power device: Experiment validation and numerical simulation," Compos Part B Eng, vol. 281, no. February, p. 111519, 2024, doi: 10.1016/j.compositesb.2024.111519.

[48] N. Heuck et al., "Aging of new Interconnect-Technologies of Power-Modules during Power-Cycling," CIPS 2014 - 8th Int Conf Integr Power Electron Syst, pp. 25–27, 2014.

[49] J. Dai, J. Li, P. Agyakwa, M. Corfield, and C. M. Johnson, "Comparative thermal and structural characterization of sintered nano-silver and high-lead solder die attachments during power cycling," IEEE

Trans Device Mater Reliab, vol. 18, no. 2, pp. 256–265, 2018, doi: 10.1109/TDMR.2018.2825386.

[50] P. Agyakwa et al., "Three-dimensional damage morphologies of thermomechanically deformed sintered nanosilver die attachments for power electronics modules," J Microsc, vol. 277, no. 3, pp. 140–153, 2020, doi: 10.1111/jmi.12803.

[51] K. Hosoya, Y. Kariya, H. Sugimoto, and K. Takahashi, "Fatigue Crack Networks in the Die-Attach Joint of a Power Semiconductor Module During Power Cycling Testing and Effects of Test Parameters on the Joint Fatigue Life," J Electron Mater, vol. 49, no. 10, pp. 6175–6186, 2020, doi: 10.1007/s11664-020-08381-7.

[52] S. Liu et al., "Fatigue Crack Networks in Die-Attach Layers of IGBT Modules Under a Power Cycling Test," IEEE Trans Power Electron, vol. 39, no. 12, pp. 16695–16707, 2024, doi: 10.1109/TPEL.2024.3447909.

[53] X. Long, Y. Guo, Y. Su, K. S. Siow, and C. Chen, "Constitutive, creep, and fatigue behavior of sintered Ag for finite element simulation of mechanical reliability: a critical review," J Mater Sci Mater Electron, vol. 33, no. 5, pp. 2293–2309, 2022, doi: 10.1007/s10854-021-07474-1.

[54] H. Tatsumi, S. Kumada, A. Fukuda, H. Yamaguchi, and Y. Kashiba, "Impact of metallurgical and mechanical properties of sintered silver joints on die-attach reliability of high-temperature power modules," J Microelectron Electron Packag, vol. 13, no. 3, pp. 121–127, 2016, doi: 10.4071/imaps.506.

[55] K. Wakamoto, T. Otsuka, K. Nakahara, V. Mugilgeethan, R. Matsumoto, and T. Namazu, "Degradation Mechanism of Silver Sintering Die Attach Based on Thermal and Mechanical Reliability Testing," IEEE Trans Components, Packag Manuf Technol, vol. 13, no. 2, pp. 197–210, 2023, doi: 10.1109/TCPMT.2023.3242423.

[56] Y. Su, G. Fu, C. Liu, C. Liu, and X. Long, "Fatigue crack evolution and effect analysis of Ag sintering die-attachment in SiC power devices under power cycling based on phase-field simulation," Microelectron Reliab, vol. 126, no. May, p. 114244, 2021, doi: 10.1016/j.microrel.2021.114244.

[57] S. Zhang, Q. Wang, T. Lin, P. Zhang, P. He, and K. W. Paik, "Cu-Cu joining using citrate coated ultra-small nano-silver pastes," J Manuf Process, vol. 62, no. November 2020, pp. 546–554, 2021, doi: 10.1016/j.jmapro.2020.11.043.

[58] F. Zhou et al., "Demonstration of Avalanche and Surge Current Robustness in GaN Junction Barrier Schottky Diode with 600-V/10-A Switching Capability," IEEE Trans Power Electron, vol. 36, no. 11, pp. 12163–12167, 2021, doi: 10.1109/TPEL.2021.3076694.

[59] G. Zeng, F. Wenisch-Kober, and J. Lutz, "Study on power cycling test with different control strategies," Microelectron Reliab, vol. 88–90, no. May, pp. 756–761, 2018, doi: 10.1016/j.microrel.2018.07.088.

[60] Z. Zhang et al., "Online Condition Monitoring of Solder Fatigue in a Clip-Bonding SiC mosfet Power Assembly via Acoustic Emission Technique," IEEE Trans Power Electron, vol. 38, no. 2, pp. 1468–1478, 2023, doi: 10.1109/TPEL.2022.3209740.

[61] X. Zhang et al., "A Method for Improving the Thermal Shock Fatigue Failure Resistance of IGBT Modules," IEEE Trans Power Electron, vol. 35, no. 8, pp. 8532–8539, 2020, doi: 10.1109/TPEL.2019.2963236.

[62] E. Kondakci and N. Solak, "Enhanced thermal conductivity and long-term stability of diamond/aluminum composites using SiC-coated diamond particles," J Mater Sci, vol. 57, no. 5, pp. 3430–3440, 2022, doi: 10.1007/s10853-021-06817-x.

[63] M. T. Lee, M. H. Fu, J. L. Wu, C. Y. Chung, and S. J. Lin, "Thermal properties of diamond/Ag composites fabricated by eletroless silver plating," Diam Relat Mater, vol. 20, no. 2, pp. 130–133, 2011, doi: 10.1016/j.diamond.2010.11.017.

[64] Y. Zhu et al., "Multiple valence bands convergence and strong phonon scattering lead to high thermoelectric performance in p-type PbSe," Nat Commun, vol. 13, no. 1, pp. 1–9, 2022, doi: 10.1038/s41467-022-31939-4.

[65] Q. Ren et al., "Establishing the carrier scattering phase diagram for ZrNiSn-based half-Heusler thermoelectric materials," Nat Commun, vol. 11, no. 1, pp. 1–9, 2020, doi: 10.1038/s41467-020-16913-2.

[66] E. Çadirli, U. Böyük, H. Kaya, N. Maraşli, S. Aksöz, and Y. Ocak, "Dependence of electrical resistivity on temperature and Sn content in Pb-Sn solders," J Electron Mater, vol. 40, no. 2, pp. 195–200, 2011, doi: 10.1007/s11664-010-1425-8.

[67] D. Kim, S. Lee, C. Chen, S. J. Lee, S. Nagao, and K. Suganuma, "Fracture mechanism of microporous Ag-sintered joint in a GaN power device with Ti/Ag and Ni/Ti/Ag metallization layer at different thermo-mechanical stresses," J Mater Sci, vol. 56, no. 16, pp. 9852–9870, 2021, doi: 10.1007/s10853-021-05924-z.

[68] J. Cheng, G. Song, Z. Zhang, M. S. Khan, Z. Liu, and L. Liu, "Improving heat-affected zone softening of aluminum alloys by in-situ cooling and post-weld rolling," J Mater Process Technol, vol. 306, no. May, p. 117639, 2022, doi: 10.1016/j.jmatprotec.2022.117639.

[69] S. K. Lee, S. B. Lee, S. Y. Park, Y. S. Yi, and C. W. Ahn, "Structure of amorphous aluminum oxide," Phys Rev Lett, vol. 103, no. 9, pp. 4–7, 2009, doi: 10.1103/PhysRevLett.103.095501.

[70] H. Yang et al., "A new insight into heterogeneous nucleation mechanism of Al by non-stoichiometric TiCx," Acta Mater, vol. 233, p. 117977, 2022, doi: 10.1016/j.actamat.2022.117977.

[71] H. Zhang et al., "Physical process-aided fabrication of periodic Au-M (M = Ag, Cu, Ag-Cu) alloyed nanoparticle arrays with tunable localized surface plasmon resonance and diffraction peaks," RSC Adv, vol. 8, no. 17, pp. 9134–9140, 2018, doi: 10.1039/c7ra13567j.

[72] P. A. Agyakwa et al., "Microstructural Response of Highly Porous Sintered Nano-silver Particle Die Attachments to Thermomechanical Cycling," J Electron Mater, vol. 53, no. 3, pp. 1374–1398, 2024, doi: 10.1007/s11664-023-10870-4.

[73] X. Zhang, Y. Ji, L. Q. Chen, and Y. Wang, "First-principles calculations of γ-Al_2O_3/Al interfaces," Acta Mater, vol. 252, no. April 2022, p. 118786, 2023, doi: 10.1016/j.actamat.2023.118786.